University of Tasmania Open Access Repository

Cover sheet

Title

Gold and trace element zonation in pyrite using a laser imaging technique: Implications for the timing of gold in orogenic and Carlin-style sediment-hosted deposits

Author

Ross Large, Leonid Danyushevsky, Hollitt, CP, Maslennikov, V, Sebastien Meffre, Gilbert, SE, Stuart Bull, Robert Scott, Emsbo, P, Thomas, HV, Singh, B, Foster, J

Gold and Trace Element Zonation in Pyrite Using a Laser Imaging Technique: Implications for the Timing of Gold in Orogenic and Carlin-Style Sediment-Hosted Deposits

Ross R Large,[1,†] Leonid Danyushevsky,[1] Chris Hollit,[1] Valeriy Maslennikov,[2] Sebastien Meffre,[1] Sarah Gilbert,[1] Stuart Bull,[1] Rob Scott,[1] Poul Emsbo,[3] Helen Thomas,[1] Bob Singh,[4] and Jeffrey Foster[1]

[1]*CODES ARC Centre of Excellence in Ore Deposits, Private Bag 126, University of Tasmania, Australia 7001*

[2]*Institute of Mineralogy, Russian Academy of Science, Urals Branch, Miass, Russia*

[3]*U.S. Geological Survey, Mail Stop 973, Denver, Colorado 80225*

[4]*Skygold Ventures, 615-800 West Pender St. Vancouver, British Columbia, Canada V6C 2V6*

Abstract

Laser ablation ICP-MS imaging of gold and other trace elements in pyrite from four different sediment-hosted gold-arsenic deposits has revealed two distinct episodes of gold enrichment in each deposit: an early synsedimentary stage where invisible gold is concentrated in arsenian diagenetic pyrite along with other trace elements, in particular, As, Ni, Pb, Zn, Ag, Mo, Te, V, and Se; and a later hydrothermal stage where gold forms as either free gold grains in cracks in overgrowth metamorphic and/or hydrothermal pyrite or as narrow gold-arsenic rims on the outermost parts of the overgrowth hydrothermal pyrite. Compared to the diagenetic pyrites, the hydrothermal pyrites are commonly depleted in Ni, V, Zn, Pb, and Ag with cyclic zones of Co, Ni, and As concentration. The outermost hydrothermal pyrite rims are either As-Au rich, as in moderate- to high-grade deposits such as Carlin and Bendigo, or Co-Ni rich and As-Au poor as in moderate- to low-grade deposits such as Sukhoi Log and Spanish Mountain. The early enrichment of gold in arsenic-bearing syngenetic to diagenetic pyrite, within black shale facies of sedimentary basins, is proposed as a critical requirement for the later development of Carlin-style and orogenic gold deposits in sedimentary environments. The best grade sediment-hosted deposits appear to have the gold climax event, toward the final stages of deformation-related hydrothermal pyrite growth and fluid flow.

Introduction

Current theories on orogenic gold deposits maintain that the gold is introduced from a deeply sourced fluid late in the deformation history of the deposit (syn- or postkinematic; Groves et al., 2000; Hagemann and Cassidy, 2000). Our study of the compositional zoning of pyrite in several sediment-hosted orogenic and Carlin-style gold deposits, using a new technique of LA-ICPMS imaging, shows that invisible gold is concentrated early in the pyrite, along with a specific suite of other trace elements (As, Ni, Pb, Zn, Mo, Te, V, Se), during the growth of diagenetic pyrite, and may be remobilized and reconcentrated late, in the outer growth zones of hydrothermal pyrite, toward the final stages of deformation.

Studies of modern sediments in lakes and ocean basins have demonstrated that Fe sulfides begin to grow within the first few millimeters of the sediment-water interface at the bottom of basins as a result of the depletion of oxygen in the uppermost sediments by biogenic activity (Scholtz and Neuman, 2007) and the activity of sulfate-reducing bacteria (Schieber, 2002; Folk, 2005). The pyrite formed in this environment tends to be fine grained and enriched in base metals and various other trace elements including Zn, Cu, Cd, V, Cr, Co, and As. These trace elements are considered to be released from the clasts in the sediments, both before and during reduction, and eventually incorporated into the diagenetic pyrite (Morse and Luther, 1999; Scholtz and Neuman, 2007). Experimental studies have also shown that low-temperature

(<150°C) pyrites that formed rapidly are more likely to be fine grained and framboidal in shape compared to pyrite crystals that formed more slowly and at a higher temperature (>200°C) from hydrothermal or metamorphic fluids (Butler and Rickard, 2000). These metamorphic and/or hydrothermal pyrites are expected to be coarser grained and less enriched in trace elements due to the higher temperature and slower growth of pyrite, which allows the trace elements to be partitioned into separate sulfide phases rather than incorporated into pyrite in solid solution or as very small (<5μm) inclusions. During metamorphism new pyrite either undergoes recrystallization (Wagner and Boyce, 2006; Heiligmann et al., 2008) or overgrows earlier pyrite (Large et al., 2007), depending on the physical and chemical environment during metamorphism.

These textural and chemical differences between pyrite types, coupled with the laser imaging technique described in this study, and the tendency for later hydrothermal pyrite to form growth zones on earlier sedimentary and diagenetic pyrite crystals, allows Au and other metals to be traced throughout the history of formation of sediment-hosted Au deposits. In this study, we have investigated the textures and compositional trace element zoning of pyrite in selected pyritic shale samples associated with the following four sediment-hosted gold deposits: Sukhoi Log in Siberia, Bendigo in Victoria, Spanish Mountain in British Columbia, and the northern Carlin Trend in Nevada. The deposits are hosted by carbonaceous sedimentary rocks, typically black shales, with a variable carbonate component. Sukhoi Log, Bendigo, and Spanish Mountain occur in metamorphosed and moderately

---

† E-mail: Ross.Large@utas.edu.au

to strongly deformed basins and have been referred to as oro-genic gold deposits (e.g., Groves et al., 1998). By contrast, the Carlin deposits occur in a deformed but less metamorphosed sedimentary environment (Hofstra and Cline, 2000). These four deposits were selected for study because they are hosted by carbonaceous sediments and contain disseminated sedi-mentary and hydrothermal pyrite, which is amenable to LA-ICPMS trace element mapping. One of the major aims of this project was to compare the textures and trace element pat-terns in the sedimentary diagenetic pyrite with those in the synore, hydrothermal pyrite. A comprehensive study of trace element distributions in all pyrite generations for each of the four deposits is beyond the scope of this paper, however, we aim to provide textural and LA-ICPMS data and comments on a selected group of pyrite types from each deposit.

Several previous studies of pyrite chemistry have demon-strated the common zonation of As, Co, and Ni in different pyrite types, revealed by microprobe analysis and X-ray and backscatter electron imaging (e.g., Craig et al., 1998; Fleet et al., 1993). Many trace elements in pyrite (e.g., Au, Ag, Pb, Mo, Se, Bi, Te) are typically present at levels too low (below about 50 ppm) to be easily detected by microprobe and SEM, and it has not been until the development of PIXIE, SIMS, and LA-ICPMS that this suite of elements has been available for study in pyrite (e.g., Griffin et al., 1991; Huston et al., 1995; Cline et al., 2003; Emsbo et al., 2003; Reimold et al., 2004; Chouinard et al., 2005; Benzaazoua et al., 2007; Large et al., 2007; Wagner et al., 2007). Previous investigations (e.g., Bakken et al., 1989; Cabri et al., 1989; Cook and Chryssoulis 1990; Fleet et al., 1993; Deditius et al., 2009) have shown that submicroscopic gold, termed invisible gold, can be present in arsenian pyrite and arsenopyrite in solid solution in the crystal structure and/or as discrete minute particles. Gold is preferentially concen-trated in arsenic-rich zones of arsenian pyrite in a range of ore deposit types (e.g., Fleet et al., 1993; Mumin et al., 1994; Cline et al., 2003). Reich et al. (2005) have shown that the maximum amount of gold that can be dissolved in the structure of arsen-ian pyrite depends on the arsenic content of pyrite, according to the equation: $C_{Au} = 0.02 \times C_{As} + 4 \times 10^{-5}$. The line de-scribed by this equation is referred to as the gold saturation line for pyrite. Below this line, gold can be present as invisible gold in the structure of arsenian pyrite, whereas above the line, free gold or gold tellurides are present as blebs within the pyrite.

Imaging of element distribution patterns within minerals using a multicollector LA-ICPMS technique has recently been demonstrated (e.g., Woodhead et al., 2007), and in this paper we provide the first results from a quadrapole LA-ICPMS imaging technique, which enables a suite of trace el-ements to be simultaneously measured across the surface of pyrite grains. The low detection limit and simultaneous cap-ture of data for up to 20 trace elements make this a powerful analytical tool for understanding pyrite genesis and evolution. This technology allows the mapping of both invisible gold and gold particles within pyrite and thus a comparison of gold dis-tribution with pyrite texture and the zoning of other trace el-ements in the pyrite. LA-ICPMS mapping cannot determine whether invisible gold occurs dissolved in the structure of pyrite or is present as microinclusions (less than 0.1 μm across) in the pyrite as recently demonstrated by Deditius et al. (2009). However, irrespective of this limitation, LA-ICPMS

mapping of trace elements in ores now provides a rapid and robust technique for determining the place of gold in the sul-fide paragenesis of gold ore deposits. Previous techniques re-lied on free gold, which due to its soft and easily malleable na-ture and tendency to move into late fractures, is an unreliable informer of paragenetic place and ultimate timing of gold in-troduction into an ore deposit (Mumin et al., 1994).

Analytical Techniques

The instrumentation used in this study includes a New Wave 213-nm solid-state laser microprobe coupled to an Ag-ilent 4500 quadrupole ICPMS housed at the CODES LA-ICPMS analytical facility, University of Tasmania.

The laser microprobe was equipped with an in-house small volume (~2.5 cm^3) ablation cell characterized by <1-s response time and <2-s wash-out time. Ablation was performed in an at-mosphere of pure He (0.7 l/min). The He gas carrying the ab-lated aerosol was mixed with Ar (1.23 l/min) immediately after the ablation cell and the mix is passed through a pulse-homog-enizing device prior to direct introduction into the torch.

The ICPMS was optimized daily to maximize sensitivity on mid- to high-mass isotopes (in the range 130–240 a.m.u.). Production of molecular oxide species (i.e., $^{232}Th^{16}O/^{232}Th$) and doubly charged ion species (i.e., $^{140}Ce^{2+}/^{140}Ce^{+}$) was maintained at <0.2 percent. Due to the low level of molecu-lar oxide and doubly charged ion production, no correction was introduced to the analyte signal intensities for such po-tential interfering species. Each analysis was performed in the time-resolved mode, which involves sequential peak hopping through the mass spectrum.

Quantitative multielement analysis of sulfides

For this study, the quantitative pyrite analyses were per-formed by ablating spots ranging in size from 25 to 40 μm. Laser repetition rate was typically 5 HZ and laser beam en-ergy at the sample was maintained between 4 and 5 J/cm^2. The analysis time for each sample was 100 s, comprising a 30-s measurement of background (laser off) and a 70-s analysis with laser on. Acquisition time for most masses was set to 0.02 s, however, major silicate elements (Mg, Al, Si, Ca) and S were measured for 0.005 s, trace silicate elements (Zr, Ba, La, Th, U) and Cd for 0.01 s, Se, Mo, and Ag for 0.1 s, Te for 0.2 s, and Au for 0.4 s, with a total sweep time of ~1.5 s. Data re-duction was undertaken according to standard methods (Lon-gerich et al., 1996) using Fe as the internal standard. An in-house Li borate fused glass of a pyrite and/or sphalerite mixture (Danyushevsky et al., in press) was used as the pri-mary calibration standard. The standard was analyzed twice every one and a half hours to account for the instrument drift, with a 100-μm beam and at 10 Hz.

The precision of trace element analysis by LA-ICPMS is rarely better than 5 percent (Danushevsky et al., in press). Thus variations in the internal standard concentrations of 5 percent are within the noise. Fe concentration in pyrite normally varies by less than 5 percent of the stoichiometric value. For exam-ple, 34 electron microprobe analyses of Carlin pyrite from the Meikle deposit by Embso et al. (2003) show a variation in Fe content from 43.16 to 46.97 wt percent (stoichiometric Fe = 45.3 wt %), and As from 0.40 to 7.51 wt percent. The variation in Fe is within ±2.2 wt percent and, thus, less than

the analytical error of 5 percent. On this basis, no correction was applied for variations in the Fe internal standard, even when As content of the pyrite was above 5 wt percent.

Imaging of sulfides

Imaging was performed by ablating sets of parallel lines in a grid across the samples. Depending on the sample size, lines were ablated with a beam size of 15 or 25 μm. The spacing between the lines was kept constant at the same size as the laser beam. The lines were ablated with the repetition rate of 10 Hz, rastering at 15 or 25 μm/s, depending on the spot size. Thus, every position in the sample was ablated 10 times and its composition contributed to 5 consecutive pixels in the image, resulting in an unprocessed effective resolution matching the beam size. Every sweep recorded in the mass spectrometer forms a separate pixel in the map. For a normal sweep time of ~0.2 s, with an image speed of 25 μm/s, one pixel equals 5 μm.

Depth of ablation during mapping was around 5 μm. This is estimated from the known depth of ablation by a single shot (0.5 μm) and the known number of shots in a single point in pyrite (10), which is determined by the relationship between the speed with which the sample moves under the laser beam and the spot size used.

A set of 20 elements was analyzed with acquisition time for most masses set to 0.002 s, however, to improve their detection limits, Se was measured for 0.004 s and Ag, Te, and Au for 0.04 s. The total sweep time was ~0.2 s. To allow for cell wash-out, a delay of 13 s was used after each line. Background levels and the primary sulfide standard (Danyushevsky et al., in press) were measured before and after each image.

Typically images were analyzed over 1 to 2 h where sensitivity drift was negligible. Standards were analyzed immediately before and after the image to assess drift. Images were corrected for drift when necessary, but not routinely, and drift is assumed to be linear between the two sets of standards.

Image processing involved: (1) ICPMS sensitivity drift was corrected for each element individually, based on the standard measurements before and after image acquisition; (2) a median filter was applied to remove spikes originating from counting statistics; (3) the average background for each element was subtracted from the filtered counts; (4) for each element, background-corrected counts that were below the standard deviation on the average background were assigned the standard deviation value; and (5) images were then produced for each element using a logarithmic color scale.

The effect of redeposition during mapping was minimized by preablating each line prior to the main mapping burn. However, this does not remove the redeposited material completely. In our experience the redeposition can be a factor when looking at variation of concentrations of two to three times in an area where concentration can vary by several orders of magnitude. On images with a concentration scale of several orders of magnitude (as those presented here), redeposition is generally not an issue; however, some Au noise is evident on some maps around large native gold inclusions.

Gold imaging in pyrite

The mapping technique enables gold distribution in pyrite to be determined; both low-level invisible gold (0.01–5,000 ppm Au) or discrete inclusions of free gold or gold-bearing telluride minerals. Unlike the transmission electron microscope, the LA-ICPMS mapping technique will not distinguish between gold present as nano particles in pyrite compared to gold present in solid solution in the pyrite structure. However, if the gold particles are of sufficient size, in the micro-, rather than nano range, they can be identified in the line data and resolved on the pyrite map. The minimum size of gold inclusions that can be detected depends on a number of factors: (1) the laser spot size, (2) the background low-level amount of gold in the pyrite, and (3) the purity (fineness) of gold in the inclusion. For a standard spot size of 25 μm, gold background of 1 ppm and 100 percent fineness inclusions, a minimum gold inclusion of 0.25 μm can be detected. The three-point filter intended to take out spurious single-point spikes may remove some of the smallest inclusions during processing. However, most inclusions will be analyzed over multiple data points (as each point on the surface is ablated 10 times) and hence will not be filtered out.

Sukhoi Log Pyrite

Sukhio Log is a 30 plus million ounce (Moz) gold deposit in the Lena gold province in Siberia, located 850 km northeast of Irkutsk (Distler et al., 2004; Wood and Popov, 2006; Chang et al., 2008). The deposit is hosted by Neoproterozoic black shales, dated by the U/Pb zircon method by Meffre et al. (2008) to have a maximum age of 600 Ma. The ores are composed of pyritic black shales with folded bedding-parallel pyrite-quartz veinlets confined to the core of an overturned anticline (Fig. 1; Distler et al., 2004; Large et al., 2007).

Pyrite types at Sukhoi Log

Five main pyrite types have been defined at Sukhoi Log (Large et al., 2007) in paragenetic sequence from pyrite 1 (py1) to pyrite 5 (py5): (1) py1 (Fig. 2A) is composed of clusters of very fine grained crystals (<3 μm) commonly aligned parallel to bedding, (2) py2 comprises slightly coarser grained euhedral pyrite from 20 to 50 μm intergrown with py1, (3) py3 (Fig. 2B) forms coarser grained subhedral to euhedral masses of pyrite (2–5 mm across) which overgrow py1 and py2, (4) py4 (Fig. 2C) forms larger (3–40 mm) euhedral crystals which contain inclusions parallel to the main deformation fabric in the shales, and (5) py5 is a clear pyrite (Fig. 2D), up to 2mm across, which overgrows py3 and py4 and was formed after the main deformation. Py1 and py2 are interpreted by Large et al. (2007) as diagenetic, py3 as late diagenetic to early metamorphic, py4 as peak deformation, and py5 as postpeak deformation. Sulfur isotope studies (Chang et al., 2008) reveal that py1 and py2 have a wide spread of δ^{34}S values from –7 to +20 per mil, with a mean of 10.5 per mil, typical of a reduced seawater sulfate source. Later sulfide generations (py3–py5) have a narrower δ^{34}S spread, but the same mean, indicating they formed by the recrystallization of previous py1 and py2, accompanied by homogenization of the S isotopes (Chang et al., 2008).

Pyrite composition and zoning at Sukhoi Log

In previous studies at Sukhoi Log (Large et al., 2007; Meffre et al., 2008), we have undertaken LA-ICPMS spot analyses on over 60 pyrite samples, both within the ore zone and the surrounding low gold grade halo (Fig. 1A). A selection of this data is presented in Table 1, with sample locations shown in Figure 1.
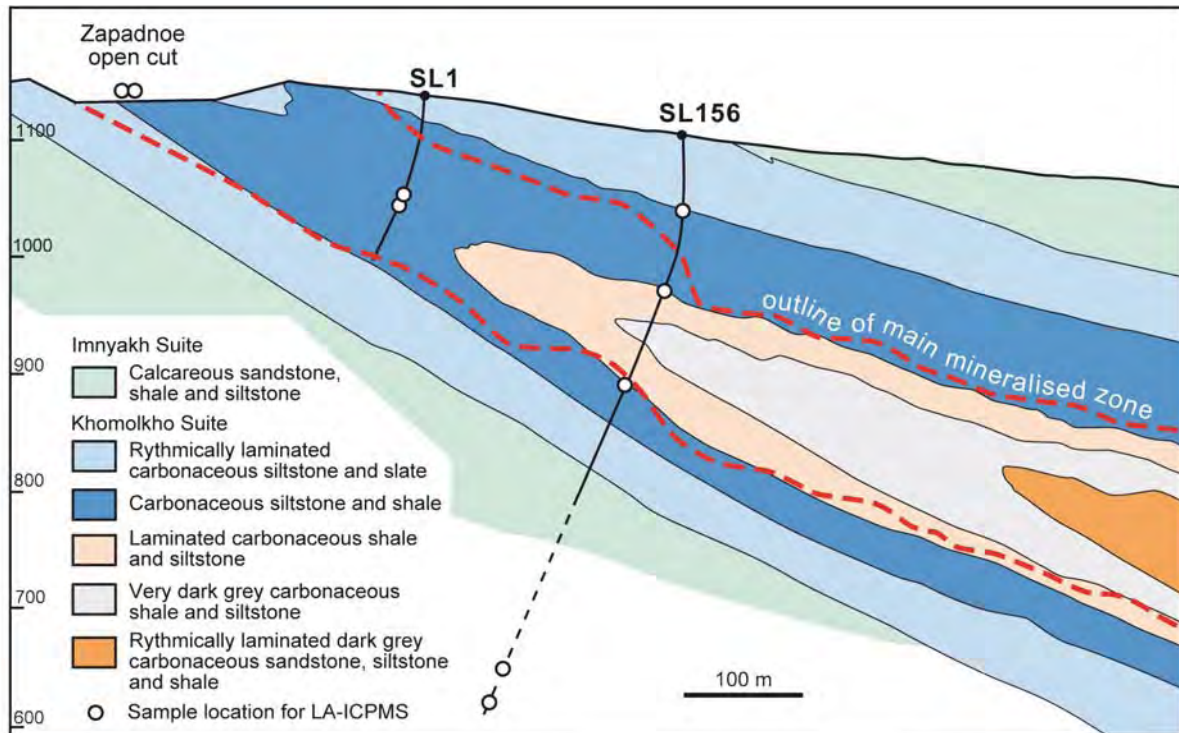
Fig 1. Schematic geologic section of Sukhoi Log, showing the positions of pyritic sediment samples used in this study (after Buryak and Khmelevskaya, 1997).

Fig 2. Textures of pyrite types at the Sukhoi Log gold deposit. A. Clusters of syndiagenetic pyrite microcrystals (py1) in black shale. B. Euhedral py3 overgrowing framboidal py1. C. Synmetamorphic py4 overgrowing the deformation fabric (LHS) and veining (RHS) in the sediment matrix. D. Zoned pyrite, composed of py3 in core and py5 in outer zone, in bedding-parallel pyrite-quartz veinlet.

TABLE 1. LA-ICPMS Analyses of Selected Pyrite Types from Sukhoi Log, Bendigo, Spanish Mountain and North Carlin Trend

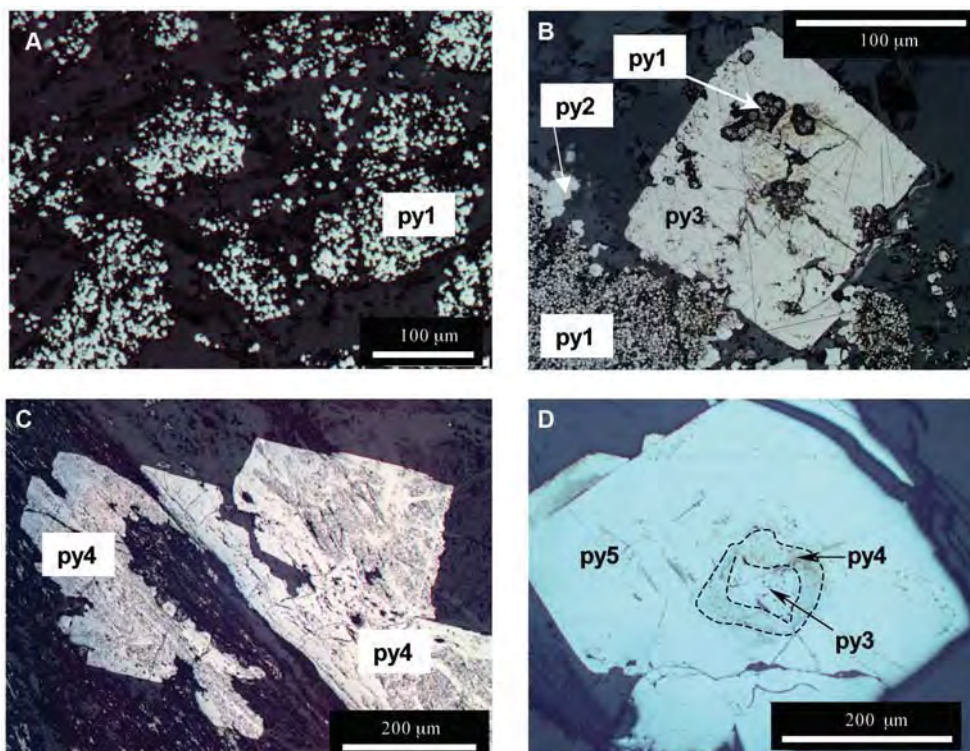| Sample no.	Analysis no.	Interpretation of timing*	Au (ppm)	Al (ppm)	Ti (ppm)	V (ppm)	Cr (ppm)	Mn (ppm)	Fe internal standard	Co (ppm)	Ni (ppm)	Cu (ppm)	Zn (ppm)	As (ppm)
Sukhoi Log														
SL-1-98.5a	FE09A26	D	0.57	6607.92	57.62	8.26	10.23	73.20	453000	144.79	148.14	34.51	113.43	582.92
SL-1-91a	FE09A13	D	0.70	7338.90	102.54	10.98	8.77	80.67	453000	190.48	209.54	40.16	136.47	718.98
SL-524/70.9-1-3	AP04A73	D	1.82	6071.87	49.35	7.22	6.89	22.41	465000	177.12	758.86	123.59	6.18	2656.73
SL-156/526-10	MA23A84	D	6.18	9246.36	291.76	45.98	21.16	306.88	465000	175.49	1021.38	227.96	90.53	3601.53
SL-156/225-C1-9	MA14A11	D	6.55	4066.04	48.95	5.98	10.71	1969.16	465000	170.80	1252.16	594.96	47.60	3273.89
SL-156/225-C2-1 fram	MA14A13	D	7.41	16171.13	159.58	22.58	26.16	1440.06	465000	263.77	1488.36	479.95	53.10	2902.15
SL-524/68.5-NC-2	AP04A94	D	5.02	29315.18	174.63	45.80	44.04	256.14	465000	2016.51	1023.10	302.24	36.10	3043.60
SL-176/300-19	MA23A49	D	7.47	21692.82	178.88	68.77	83.36	270.56	465000	150.36	598.65	328.20	69.23	1425.18
SL-C59/240-2-3	AP04A38	D-M	0.12	2427.07	61.35	2.38	1.36	96.29	465000	40.98	1298.50	6767.91	94.10	301.46
SL-C-59-210	FE09A52	D-M	0.13	5259.49	674.13	13.95	19.51	19.72	454000	14.92	460.30	375.17	18.35	1529.37
SL-156/225-C2-1 py	MA14A13	D-M	<0.20	0.70	14.08	0.10	2.30	4.20	465000	140.67	1716.69	1.80	2.20	4716.22
SL-524/81-C3-1	MA14A64	D-M	0.36	2232.53	1558.53	5.41	11.14	100.40	465000	45.73	933.69	28.67	6.36	2917.82
SL-97/390.5B-C2-1	MA14A78	D-M	<0.05	382.46	96.53	1.08	2.30	1.62	465000	0.29	410.92	3.25	2.20	1721.15
SL-156/225-C1-2	MA14A04	D-M	<0.22	1.07	23.01	0.10	2.30	1.00	465000	242.29	1504.22	1.80	2.20	4385.99
SL-C59/240-3-3	AP04A41	MH	0.03	160.50	32.88	0.25	2.30	0.62	465000	49.97	54.71	1.73	1.36	1441.04
SL-156/55.5-2-3C	AP04A61	MH	0.31	1652.96	3481.68	6.55	9.00	5.73	465000	3.58	484.96	411.29	2.20	1658.20
SL-524/22.5-C1-2	MA14A26	MH	0.82	5941.60	1925.69	11.28	17.49	2.29	465000	5.84	402.65	184.88	2.73	1728.27
SL-156/135.5-C2-1	MA14A56	MH	0.04	25.39	782.11	0.68	2.30	27.94	465000	15.16	24.45	1.80	2.20	2362.42
SL-524/22.5-C2-3	MA14A34	MH	1.30	3305.77	569.20	4.99	9.12	10.56	465000	188.15	560.09	29.27	2.30	3365.07
SL-1-99.5a	FE09A30	MH	0.00	0.95	5.55	0.02	2.30	0.95	465000	0.93	18.42	0.55	0.34	979.15
SL-1-99.5a	FE09A36	MH	0.21	86.45	5.97	0.13	0.26	0.95	465000	130.33	80.51	0.06	0.48	1325.60
SL-156/490-C1-2	MA14A67	MH	0.05	0.15	8.78	0.10	2.30	1.00	465000	36.73	518.23	1.80	2.20	4315.65
Bendigo														
NBD171-377.7B-6	AP18A18	D	0.76	1896.44	48.10	4.54	6.40	7.26	465000	88.95	1858.49	3304.13	48.70	635.17
NBD171-377.7B-7	AP18A19	D	0.26	318.63	27.08	0.67	1.18	1.19	465000	28.24	1704.48	2519.01	31.57	446.84
NBD171-377.7B-8	AP18A20	D	0.70	2467.97	164.01	5.57	8.27	3.35	465000	238.94	2771.48	3725.69	53.94	1865.46
NBD161-454.3 C2-3	AP08A43	D	1.62	15027.28	1752.78	31.13	79.41	47.33	465000	767.16	893.63	40.68	21.46	3954.74
NBD161-437.15-C2-4	AP02A42	D	1.45	25620.49	1150.44	33.94	75.94	104.36	465000	3118.95	610.65	119.90	69.87	840.46
NBD171-377.7B-4	AP18A16	MH	0.31	502.51	664.00	1.44	4.00	0.55	465000	440.26	2524.16	15.75	16.19	820.78
NBD171-377.7B-13	AP18A25	MH	0.27	355.96	1021.96	1.63	4.74	0.50	465000	1125.95	2849.85	28.42	0.73	2144.01
NBD171-544.8 C2-9	AP08A72	MH	0.04	51.83	195.21	0.12	<3.33	0.60	465000	9.70	3.87	4.19	0.90	67.53
NBD161-431.3 C2-3	AP02A17	MH	0.59	15865.80	7448.70	24.32	83.80	47.31	465000	807.54	642.10	21.63	18.83	946.01
NBD171-377.7B-2	AP18A13	MHR	2.73	855.69	1388.45	3.00	7.05	1.31	465000	19.34	138.26	22.12	1.36	6047.12
NBD171-377.7B-2a	AP18A14	MHR	3.39	1263.07	2798.22	4.50	15.33	1.40	465000	72.30	280.85	27.62	8.41	5908.26
NBD171-377.7B-3	AP18A15	MHR	6.08	432.50	1563.58	2.51	4.51	0.87	465000	9.23	76.05	35.62	1.19	8505.70
NBD161-448.8-C1-1	AP08A10	MHR	26.98	4.64	6.75	0.06	<5.09	1.00	465000	0.67	10.57	9.80	0.90	16510.58
NBD161-448.8-C1-4	AP08A13	MHR	17.52	1.75	9.33	0.15	<7.63	2.20	465000	6.66	89.22	20.75	1.40	12883.51

TABLE 1. (Cont.)

Sample no.	Analysis no.	Interpretation of timing*	Au (ppm)	Al (ppm)	Ti (ppm)	V (ppm)	Cr (ppm)	Mn (ppm)	Fe internal	Co (ppm)	Ni (ppm)	Cu (ppm)	Zn (ppm)	As (ppm)
Spanish Mountain														
SM1-79.8-A-8	JA17B09	D	3.85	556.92	221.70	1.70	<3.09	3.42	465000	11.17	2896.28	2262.03	156.48	11606.61
SM1-79.8-B-1	JA17B15	D	9.51	157.56	13.85	0.68	<3.09	<1.32	465000	28.00	2827.98	584.84	234.25	11180.54
SM1-79.8-A-9	JA17B07	D	10.69	313.44	217.50	0.84	<3.09	1.61	465000	2.89	88.37	1601.84	138.37	11393.24
SM1-79.8-A-9a	JA17B08	D	10.82	1177.57	83.92	4.23	<29.33	<9.67	465000	<3.38	26.48	1221.96	31.57	12718.12
SM1-79.8-B-L6	JA17B05	D	10.02	789.93	62.32	7.02	4.52	<1.32	465000	17.87	3095.19	708.73	38.28	13968.64
SM1-79.8-A-L12	JA17B03	D	4.54	2011.81	419.58	5.52	9.37	5.76	465000	46.87	2003.67	2541.50	195.05	5908.53
SM1-79.8-B-3	JA17B13	D-M	0.70	12353.42	437.39	54.42	55.55	5.04	465000	3.41	21.89	19.83	3.76	4434.28
SM1-79.8-A-13	JA17B10	D-M	0.73	9372.07	119.57	50.45	24.44	3.94	465000	414.40	275.67	14.34	3.42	6031.54
SM1-79.8-B-2	JA17B14	D-M	0.89	6985.91	143.81	36.99	23.33	3.75	465000	9.91	29.45	11.35	2.87	5119.08
SM1-79.8-B-5	JA17B16	D-M	1.12	13004.51	324.51	63.54	59.41	5.98	465000	96.23	177.14	19.35	8.57	4862.47
SM1-79.8-B-4	JA17B12	MH	0.09	5.33	169.68	0.28	<3.09	<1.32	465000	25.96	666.86	<2.57	<1.64	4662.89
SM1-79.8-A-10	JA17B06	MH	0.13	10.87	121.32	0.30	<3.09	<1.32	465000	202.66	430.02	<2.57	<1.64	5565.58
SM1-79.8-B-8	JA17B17	MH	0.14	0.81	6.48	<0.14	<3.09	<1.32	465000	<0.44	10.54	<2.57	<1.64	5557.79
SM1-79.8-A-11	JA17B11	MH	0.17	16.84	167.70	0.33	<3.09	<1.32	465000	1.22	8.08	<2.57	<1.64	4543.83
SM1-20.5-1	JA17B20	MH	0.01	<1.62	6.99	0.07	<3.09	0.60	465000	0.22	12.12	0.13	0.80	2621.00
SM1-20.5-2	JA17B21	MH	0.17	176.33	152.27	0.78	<3.09	0.60	465000	97.65	48.04	14.33	0.80	2323.00
SM1-20.5-5	JA17B22	MH	0.07	2096.66	32.98	4.44	6.77	31.07	465000	2.08	10.73	5.18	5.56	2831.00
SM1-20.5-6	JA17B23	MH	0.17	172.79	17.11	0.46	<3.09	0.60	465000	59.39	47.27	9.56	0.80	3472.00
North Carlin Trend														
R11-156-4-225-1-1	AU21A03	D-UM	10.60	1950.36	269.51	2691.56	1185.40	168.83	465000	16.55	9601.35	12458.14	179.43	2454.69
R11-156-4-225-4-2	AU21A06	D-UM	72.35	3768.47	113.88	2169.82	1140.22	303.10	465000	12.68	8946.21	12590.30	1088.88	3896.45
R11-156-4-225-9-2	AU21A12	D-UM	168.71	10488.63	144.99	4542.47	437.82	891.15	465000	2.91	2987.64	2301.23	1333.24	5623.42
R11-156-4-225-15-1	AU21A22	D-UM	15.78	2895.74	648.97	3320.86	1056.59	235.47	465000	4.92	3885.64	11232.41	132.82	2085.42
R11-156-4-224-2-1	AU21A28	D-UM	9.54	5780.40	103.33	859.22	263.57	830.99	465000	6.80	3667.59	3502.28	973.97	3282.25
R11-156-4-224-3-2	AU21A32	D-UM	20.28	6922.84	81.99	1843.82	381.65	1039.77	465000	4.27	1169.42	865.14	3409.91	6575.11
R11-156-4-224-7-4	AU21A41	D-UM	16.37	485.55	36.31	883.05	524.01	480.57	465000	18.55	8035.61	10290.81	255.04	3629.86
M-EX92_904_1b	FE15A03	HR	207.35	3637.65	10.40	1.10	9.56	6.82	465000	84.04	70.41	399.05	8.11	14753.10
M-EX92_904_1b	FE15A04	HR	131.99	1517.28	74.71	0.14	<9	3.75	465000	155.40	90.48	817.58	0.43	73146.30
M-EX92_904_3d	FE15A13	HR	338.48	69878.16	139.44	57.40	66.36	<1	465000	71.11	32.76	403.89	8.12	15444.69
M-EX92_904_3e	FE15A15	HR	52.74	2131.05	161.26	3.35	-6.58	<17	465000	56.79	43.18	736.71	2.86	52070.96
M-DOL(ii)_1b	FE15A49	HR	1510.08	147.48	55.21	1.52	28.56	57.22	465000	1.76	48.63	860.97	23.41	73835.03
M-DOL(ii)_3a	FE15A52	HR	1620.56	77.71	4.16	2.82	<3	25.52	465000	1.49	7.12	521.60	21.57	41608.83
M-DOL(ii)_4c	FE15A56	HR	1858.61	855.39	<27	<3	<38	27.76	465000	<5	23.81	1194.65	12.45	69806.30
M-DOL(ii)_4a	FE15A58	HR	1441.70	58.50	30.00	1.63	4.63	20.16	465000	0.43	9.97	786.06	26.51	50257.32
QRC1489-890.50-1	DE18F11	HR	42.15	1246.98	120.34	11.55	7.42	54.53	465000	0.33	22.09	86.94	1.68	4671.53
QRC1489-890.50-2	DE18F12	HR	46.94	3218.36	422.04	20.11	12.17	4.84	465000	0.68	63.23	109.26	2.77	4769.84
QRC1489-890.50-3	DE18F13	HR	148.23	2800.30	231.26	19.14	11.62	58.60	465000	1.04	103.71	265.64	4.94	10775.00
QRC1489-890.50-4	DE18F14	HR	44.84	3826.91	417.92	28.38	15.00	13.39	465000	0.60	53.21	158.06	2.81	4710.84

TABLE 1. (Cont.)

Sample no.	Se (ppm)	Zr (ppm)	Mo (ppm)	Ag (ppm)	Sn (ppm)	Sb (ppm)	Te (ppm)	Ba (ppm)	La (ppm)	W (ppm)	Pt (ppm)	Tl (ppm)	Pb (ppm)	Bi (ppm)	Th (ppm)	U (ppm)
Sukhoi Log																
SL-1-98.5a	2.82	18.40	0.72	5.20	0.47	75.79	0.38	22.15	0.04	0.20	0.01	0.53	181.94	3.50	1.97	3.27
SL-1-91a	4.71	9.40	1.10	7.06	1.18	90.88	1.66	29.31	0.03	0.33	0.01	0.36	298.52	5.23	0.31	0.97
SL-524/70.9-1-3	37.31	0.83	1.40	16.64	1.40	17.02	<1.48	86.26	<0.02	0.37	0.01	0.10	232.45	7.07	<0.01	0.03
SL-156/526-10	22.31	1.38	7.30	12.75	0.45	43.08	<9.28	85.66	<0.18	<0.38	<0.75	0.30	441.47	7.13	<0.07	0.45
SL-156/225-C1-9	4.00	1.76	30.32	16.42	1.56	77.67	<2.12	87.67	0.07	0.30	<0.13	0.25	612.16	9.11	<0.02	0.03
SL-156/225-C2-1 fram	4.00	11.31	28.73	15.49	3.65	86.84	2.47	163.38	0.06	0.94	<0.14	0.54	678.27	8.18	0.08	0.14
SL-524/68.5-NC-2	4.00	7.22	0.50	14.02	0.45	73.83	<16.44	668.63	4.50	<1.14	<1.01	0.64	590.65	20.08	0.21	0.47
SL-176/300-19	45.40	10.57	29.38	10.78	2.05	39.00	<2.95	518.64	0.61	0.73	<0.27	0.35	560.85	4.99	<0.05	2.45
SL-C59/240-2-3	40.97	1.81	0.50	18.93	0.64	11.76	0.89	2.35	0.07	0.05	0.02	0.02	17.29	2.45	0.05	0.13
SL-C-59-210	31.82	48.01	30.05	4.47	1.30	30.38	1.97	28.46	2.20	0.46	0.00	0.10	322.93	13.93	0.91	1.51
SL-156/225-C2-1 py	4.00	0.03	0.50	0.16	1.40	0.14	0.90	0.12	<0.04	<0.19	<0.13	0.02	0.19	0.02	<0.03	0.01
SL-524/81-C3-1	21.64	55.88	0.50	1.46	1.37	8.51	0.90	35.72	0.31	4.66	0.01	0.02	42.99	0.17	0.35	0.90
SL-97/390.5B-C2-1	8.51	0.24	0.50	0.55	1.51	1.60	0.65	1.84	0.00	0.17	0.02	0.02	14.52	0.93	0.01	0.02
SL-156/225-C1-2	4.00	<0.13	0.50	0.16	0.45	0.14	0.90	0.12	<0.07	<0.18	<0.26	0.02	0.59	0.02	<0.03	0.01
SL-C59/240-3-3	55.10	2.32	3.91	0.56	0.58	9.93	2.12	0.97	0.02	<0.03	<0.03	0.07	21.46	2.95	0.03	0.03
SL-156/55.5-2-3C	25.27	47.41	2.29	0.94	0.54	17.77	0.90	16.45	0.22	8.27	<0.05	0.03	63.17	1.38	0.99	1.15
SL-524/22.5-C1-2	6.41	528.22	0.50	1.18	1.14	20.38	0.90	96.64	0.07	9.99	<0.04	0.05	128.60	0.98	1.61	6.17
SL-156/135.5-C2-1	26.23	5.38	1.27	0.28	1.08	0.77	0.90	0.24	0.07	1.51	0.02	0.02	4.56	0.02	0.10	0.12
SL-524/22.5-C2-3	8.14	178.05	0.50	1.20	1.21	9.95	0.90	55.03	<0.01	3.09	<0.03	0.05	81.87	1.61	0.62	3.39
SL-1-99.5a	2.91	0.00	0.01	0.04	0.49	0.25	0.05	0.02	0.00	0.01	0.00	0.02	0.67	0.01	<0.01	0.01
SL-1-99.5a	2.77	0.00	0.50	0.07	0.51	0.42	0.62	0.36	0.00	0.02	<0.02	0.01	1.65	0.03	<0.01	0.01
SL-156/490-C1-2	58.98	<0.04	0.50	0.16	0.85	0.14	<0.65	0.12	<0.01	<0.06	<0.04	0.02	0.17	0.02	<0.00	0.01
Bendigo																
NBD171-377.7B-6	71.82	0.36	31.21	15.33	0.41	160.30	7.16	19.60	0.04	0.03	0.02	0.08	2848.67	85.59	0.05	0.02
NBD171-377.7B-7	76.47	1.46	3.81	7.16	0.27	30.95	2.10	4.30	0.04	0.01	0.02	0.02	1423.32	23.42	0.02	0.02
NBD171-377.7B-8	91.07	0.61	21.31	14.72	0.63	168.85	11.68	24.24	0.54	0.15	0.02	0.14	4118.52	105.09	0.03	0.02
NBD161-454.3 C2-3	30.61	25.13	59.75	0.35	0.99	170.20	0.98	104.13	22.10	3.91	<0.13	0.96	310.77	179.08	3.54	0.82
NBD161-437.15-C2-4	69.37	27.82	13.94	1.18	1.69	415.36	7.71	141.08	0.16	2.02	<0.06	1.80	982.01	275.43	12.45	9.68
NBD171-377.7B-4	59.54	18.22	0.12	1.43	0.26	115.29	4.16	4.04	0.12	0.76	0.02	0.46	101.64	34.79	3.51	5.42
NBD171-377.7B-13	70.87	24.08	0.12	1.25	0.26	126.28	5.20	2.75	0.99	1.00	0.02	0.37	117.74	40.82	0.64	0.42
NBD171-544.8 C2-9	82.90	1.65	0.30	0.18	<0.30	15.82	0.97	0.29	150.10	0.06	<0.13	0.02	60.19	4.51	24.46	0.61
NBD161-431.3 C2-3	24.04	99.67	0.12	0.35	2.24	84.44	2.28	190.07	2.18	10.67	<0.07	0.33	277.30	98.65	2.45	1.44
NBD171-377.7B-2	57.00	33.65	0.12	1.18	0.19	96.29	2.72	5.34	0.18	3.03	0.02	0.27	159.97	27.58	6.03	7.34
NBD171-377.7B-2a	54.86	51.34	0.12	2.11	0.54	140.20	3.77	9.91	0.30	3.54	0.02	0.54	189.25	37.88	17.79	39.53
NBD171-377.7B-3	56.76	19.02	0.12	0.44	0.23	38.60	1.36	4.18	0.63	2.59	0.02	0.09	73.12	10.13	0.91	0.71
NBD161-448.8-C1-1	<8.06	1.73	0.30	0.10	<0.42	6.74	0.36	0.29	0.11	0.55	<0.12	0.05	70.01	2.54	0.04	0.02
NBD161-448.8-C1-4	<10.27	0.06	0.43	0.31	<0.84	38.19	0.62	<0.62	<0.04	0.12	<0.14	0.06	76.99	12.68	<0.04	0.04

TABLE 1. (Cont.)

Sample no.	Se (ppm)	Zr (ppm)	Mo (ppm)	Ag (ppm)	Sn (ppm)	Sb (ppm)	Te (ppm)	Ba (ppm)	La (ppm)	W (ppm)	Pt (ppm)	Tl (ppm)	Pb (ppm)	Bi (ppm)	Th (ppm)	U (ppm)
Spanish Mountain																
SM1-79.8-A-8	94.99	45.01	3.72	24.83	<0.28	8.21	0.86	7.94	2.23	5.52	<0.08	<0.03	630.44	0.31	4.88	1.75
SM1-79.8-B-1	108.32	0.17	<0.82	10.10	<0.28	3.52	1.62	4.28	<0.01	<0.09	<0.08	<0.03	214.42	0.12	<0.02	<0.01
SM1-79.8-A-9	96.98	5.95	4.00	21.90	<0.28	5.04	1.55	3.28	0.56	13.14	<0.08	<0.03	92.96	0.04	0.61	0.25
SM1-79.8-A-9a	115.02	34.04	<6.95	15.10	<2.88	9.30	<5.95	27.46	<0.09	4.17	<0.87	<0.28	432.18	<0.17	1.83	1.10
SM1-79.8-B-L6	76.98	3.85	<0.82	8.62	<0.28	1.92	<0.71	18.59	0.02	<0.09	<0.08	0.04	181.76	0.13	1.19	0.43
SM1-79.8-A-L12	96.55	21.04	<0.82	40.06	0.51	12.91	1.26	8.12	7.48	27.54	<0.08	<0.03	166.24	0.13	1.62	0.56
SM1-79.8-B-3	115.44	165.47	<0.82	3.24	0.41	8.01	1.90	235.40	0.03	2.14	<0.08	0.20	76.16	0.76	1.85	4.11
SM1-79.8-A-13	100.96	62.40	<0.82	1.88	<0.28	3.38	1.36	212.95	0.03	0.72	<0.08	0.25	43.59	0.14	2.22	2.21
SM1-79.8-B-2	128.70	109.38	<0.82	3.35	0.29	4.99	1.85	151.80	0.04	4.65	<0.08	0.19	60.79	0.16	1.75	2.09
SM1-79.8-B-5	124.15	253.50	0.92	3.94	0.73	7.08	7.99	275.66	1.00	1.83	0.41	0.57	81.05	0.75	3.01	6.26
SM1-79.8-B-4	116.64	81.15	<0.82	0.60	<0.28	1.08	0.74	<0.21	<0.01	0.31	<0.08	<0.03	11.30	0.06	0.52	2.12
SM1-79.8-A-10	124.99	159.72	<0.82	0.44	<0.28	0.54	<0.71	<0.21	<0.01	0.57	<0.08	<0.03	8.41	0.03	2.48	3.48
SM1-79.8-B-8	137.22	0.06	<0.82	<0.17	<0.28	0.26	<0.71	<0.21	<0.01	<0.09	<0.08	<0.03	2.36	<0.02	<0.02	<0.01
SM1-79.8-A-11	115.08	38.51	<0.82	0.38	<0.28	0.62	<0.71	<0.21	<0.01	0.29	<0.08	<0.03	7.92	0.03	0.44	1.04
SM1-20.5-1	112.20	<0.04	0.41	0.08	<0.28	2.81	2.41	3.32	<0.01	0.19	<0.08	0.08	44.41	3.79	0.17	0.75
SM1-20.5-2	88.10	19.90	0.41	5.02	<0.28	2.32	0.91	4.88	<0.01	0.17	<0.08	0.07	25.50	2.98	0.24	1.68
SM1-20.5-5	93.50	43.90	0.41	1.89	<0.28	4.05	1.72	2.27	<0.01	<0.09	<0.08	<0.03	33.26	4.15	0.20	1.13
SM1-20.5-6	98.30	28.40	0.41	2.09	0.50	5.29	2.15	5.16	<0.01	0.25	<0.08	0.10	52.32	10.11	0.18	0.98
North Carlin Trend																
R11-156-4-225-1-1	3561.16	3.21	740.85	148.02	6.72	671.20	11.87	32.53	0.20	1.27	0.42	246.43	332.20	4.73	0.08	1.25
R11-156-4-225-4-2	3992.54	7.09	2657.17	174.74	4.18	822.94	14.25	37.90	1.44	16.21	0.21	291.01	433.00	4.93	0.32	3.45
R11-156-4-225-9-2	4248.38	6.87	1014.08	343.06	5.82	1239.95	13.51	47.28	0.18	2.95	<0.48	370.64	576.99	2.29	<0.19	1.32
R11-156-4-225-15-1	3081.06	3.04	452.75	112.60	2.60	531.47	10.83	29.96	5.30	2.05	0.25	181.49	265.56	4.47	1.48	1.80
R11-156-4-224-2-1	2734.64	6.02	1269.48	242.72	9.38	861.03	13.03	56.78	3.29	3.10	<0.16	263.03	340.64	2.64	0.27	34.63
R11-156-4-224-3-2	3300.52	7.10	1085.56	219.13	15.45	971.52	9.82	50.31	2.31	2.69	<0.24	253.52	333.40	1.44	0.40	3.06
R11-156-4-224-7-4	3192.03	20.96	1545.41	212.14	0.64	1122.03	16.75	28.85	0.26	1.59	<0.16	416.32	448.04	5.56	0.06	0.89
M-EX92_904_1b	44.33	111.06	5.91	284.90	5.36	2070.27	82.78	27.72	0.98	52.69	-0.12	94.24	807.91	7.21	5.82	23.63
M-EX92_904_1b	25.80	0.03	4.26	186.65	2.17	1666.80	51.53	18.81	4.41	22.38	0.14	67.42	1117.38	12.00	1.66	0.19
M-EX92_904_3d	<95	53.68	33.45	232.57	<5	1183.19	<85	458.30	0.77	72.18	<0.74	67.36	481.00	3.74	2.32	3.45
M-EX92_904_3e	4.62	0.62	12.01	108.54	0.21	615.32	18.27	15.85	0.17	16.64	-0.06	25.53	382.01	4.03	0.06	0.04
M-DOL(ii)_1b	214.32	0.24	135.57	538.13	2.99	12324.01	220.36	3.27	0.20	0.57	<0.15	1133.75	72.15	<35	0.14	0.56
M-DOL(ii)_3a	115.26	4.99	31.96	234.30	<1	6551.78	77.87	5.58	0.38	20.54	<0.68	861.93	86.21	4.06	0.24	0.37
M-DOL(ii)_4c	<95	1.68	40.98	449.15	4.32	12485.81	<250	20.14	5.18	4.41	2.95	1317.91	67.19	1.77	1.89	9.70
M-DOL(ii)_4a	54.51	2.37	136.48	620.45	6.49	13369.77	132.97	1.95	1.36	6.06	0.01	1159.54	61.28	0.00	0.45	2.70
QRC1489-890.50-1	7.18	0.25	1.97	3.86	0.56	475.47	<1.22	12.95	0.97	14.44	<0.08	103.93	118.06	0.14	0.10	0.35
QRC1489-890.50-2	11.03	376.15	4.57	6.10	1.17	567.56	<1.22	34.49	0.37	6.30	<0.08	127.43	219.05	0.19	5.12	12.34
QRC1489-890.50-3	6.04	13.73	2.65	6.29	1.37	1098.53	<1.22	33.06	0.13	7.04	<0.08	278.22	152.01	0.43	0.48	1.73
QRC1489-890.50-4	6.05	78.40	<0.796	4.61	1.20	567.75	<1.22	37.23	1.07	3.63	<0.08	142.35	127.63	0.15	1.86	7.57

* D = diagenetic, MH = metamorphic/hydrothermal, MHR = metamorphic/hydrothermal outer rim, HR = hydrothermal rim, D-M = diagenetic or early metamorphic?, D-UM = diagenetic Upper Mud metalliferous horizon

Previous LA-ICPMS spot analyses by Large et al. (2007) have shown that the early diagenetic pyrites (py1 and py2) contain higher levels of invisible gold (up to 12.5 ppm, means of 2.5 and 0.4 ppm Au), compared with the later metamorphic pyrites (py4 and py5), which contain much less invisible gold (means of 0.25 and 0.07 ppm Au). However, the late diagenetic and hydrothermal and/or metamorphic pyrites contain grains of free gold, which are interpreted to have been liberated from the early-formed arsenian pyrite during late diagenesis, metamorphism, and pyrite recrystalization (Large et al., 2007).

Two pyrite samples were mapped in detail by LA-ICPMS for this study. Sample SL 156-225 (Fig. 3) is from drill hole SL 156 at a depth of 225 meters down hole (Fig. 1). The sample consists of pyritic black carbonaceous shale and siltstone, within the low gold grade halo to the ore deposit, only a few meters from the 2 g/t Au ore boundary. Fine-grained disseminated pyrite (up to 1 mm) is concentrated in thin siltstone layers (<1 cm) within the shale. The LA-ICPMS trace element map in Figure 3 covers a cluster of framboidal py1, with minor small euhedral py2, adjacent to a large euhedral crystal of py3. The mapping shows that the py1 framboids are enriched in Au, Ni, Ag, Zn, Pb, Cu, Ba, Mn, V, Bi, and Mo. By comparison the later py3 euhedra is zoned, with concentric bands of Ni, Co, and As, but contains little detectable invisible Au or Ag, Pb, Cu, Bi, and Mo.

The second sample (SLK1-A) mapped by LA-ICPMS (Fig. 4) is from the gold ore zone in the Zapadnoe open cut at the western end of the deposit (Fig. 1). This sample consists of laminated carbonaceous shale with thin (<3 cm) folded, discontinuous, pyrite-quartz veinlets. High grades of gold occur within these folded pyrite-quartz veinlets throughout Zapadnoe and the main Sukhoi Log deposit. Buyak and Khmelevskaya (1997) reported average grades of 65 ppm Au for a selection of similar veinlets. This compares with an average of 27.5 ppm Au reported by Large et al. (2007). The veinlets are prefolding (Large et al., 2007), consisting of coarse pyrite euhedra (0.5–2 cm), typically aligned along a central band parallel to bedding, fringed by fibrous quartz oriented parallel to cleavage. Large et al. (2007) demonstrated that the pyrite in the veinlets initially nucleated along particular bedding planes in the sediments during late diagenesis and was overgrown by later euhedral pyrite and quartz fibers during deformation. The LA-ICPMS trace element map in Figure 4 is of a composite euhedral pyrite within one of the veinlets. The core of the pyrite composite contains porous py3 with small inclusions of sphalerite, chalcopyrite, pyrrhotite, and native gold. The Cu and Zn maps highlight the inclusions of sphalerite and chalcopyrite in the core. However the Pb map indicates inclusions of galena that were not visible under the microscope. The elevated and spiky nature of the Ag and Bi in the core, which mirror the Pb map, suggests that the galena inclusions contain elevated Bi and Ag. The Co, As, and Ni maps suggest that the core is actually a composite of three different composition pyrites; an anhedral Co-rich phase in the lower core (Fig. 4F), an anhedral As-Ni-rich, Co-poor phase in the upper core which contains the galena, chalcopyrite, and sphalerite inclusions, and a euhedral Ni-Co–poor overgrowth phase. Although Co is mostly depleted

in the core, it is strongly enriched in the first band of the metamorphic overgrowth. Gold is only present in the inclusion-rich py3 core of the pyrite composite, associated with the microinclusions of chalcopyrite, galena, sphalerite, and pyrrhotite. In contrast there is no significant gold (<0.05 ppm) in the py5 metamorphic overgrowth.

Chemical distinction of pyrite types at Sukhoi Log

The origin and timing of the pyrite has been interpreted from textural relationships at Sukhoi Log (Large et al., 2007). However, based on the LA-ICPMS spot and map data (Figs. 3, 4), it is possible to develop compositional criteria to assist in the distinction of pyrite types. The data in Table 1, the maps (Figs. 3, 4), and previously published analyses (Large et al., 2007) indicate that the early diagenetic pyrites (py1) generally have higher levels of Zn, Pb, Ag, Ba, Mn, Ni, Cu, Bi, Mo, and V compared with the deformation-related hydrothermal pyrites (py4 and py5; Fig. 5). For example, the data in Table 1 show that the early diagenetic py1 has mean values of 552 ppm Mn, 501 ppm Pb, 208 ppm Ba, 69 ppm Zn, 12.4 ppm Mo, and 12.2 ppm Ag compared with later metamorphic and/or hydrothermal py4 and py5, which have mean values of 6.3 ppm Mn, 38 ppm Pb, 21 ppm Ba, 1.7 ppm Zn, 1.2 ppm Mo, and 0.6 ppm Ag. Py3, based on textures, is interpreted as either late diagenetic or early metamorphic (Meffre et al., 2008) and has a composition between, but overlapping, the diagenetic and metamorphic groups (Fig. 5).

Relationship of pyrite types and zonation to evolution of the Sukhoi Log deposit

The pyrite textures and trace element zonation patterns suggest a multistage process of ore genesis at Sukhoi Log. Gold was initially concentrated in fine-grained diagenetic pyrite (py1) in the carbonaceous shales and siltstones of the Komolkho Formation along with elevated As, Ni, Mn, Pb, Ag, V, Mo, Te, Cu, and Zn. These trace elements either occurred dissolved in the diagenetic pyrite structure or as nano particles dispersed in the pyrite. During diagenesis and early metamorphism most of the py1 aggregates recrystallized to py2 and/or were overgrown by py3. These processes were accompanied by release of certain trace elements (Au, Pb, Te, Cu, and Zn) from py1 to form microinclusions of free gold, gold-silver tellurides, galena, chalcopyrite, and sphalerite in the newly formed py3 (Large et al., 2007). During deformation larger euhedral grains of As-Co-Ni-Se–bearing py4 partly replaced py3 and overgrew the main metamorphic fabric in the sediments. Finally, euhedral As-Co-Ni-Se–bearing py5 overgrew py3 and py4, both within the sediments, but more commonly within bedding-parallel folded pyrite-quartz veinlets enriched in gold. The invisible gold content of syndeformational py4 and late deformation py5 are very low compared to the previous pyrite generations, indicating that the major gold introduction event at Sukhoi Log was during diagenesis and early metamorphism. The later deformation and hydrothermal pyrite formation led to remobilization and reconcentration of gold in the core of the overturned Sukhoi Log anticline associated with py3, py4, and py5. This model is supported by Pb and S isotope studies of the various pyrite generations (Chang et al., 2008; Meffre et al., 2008).
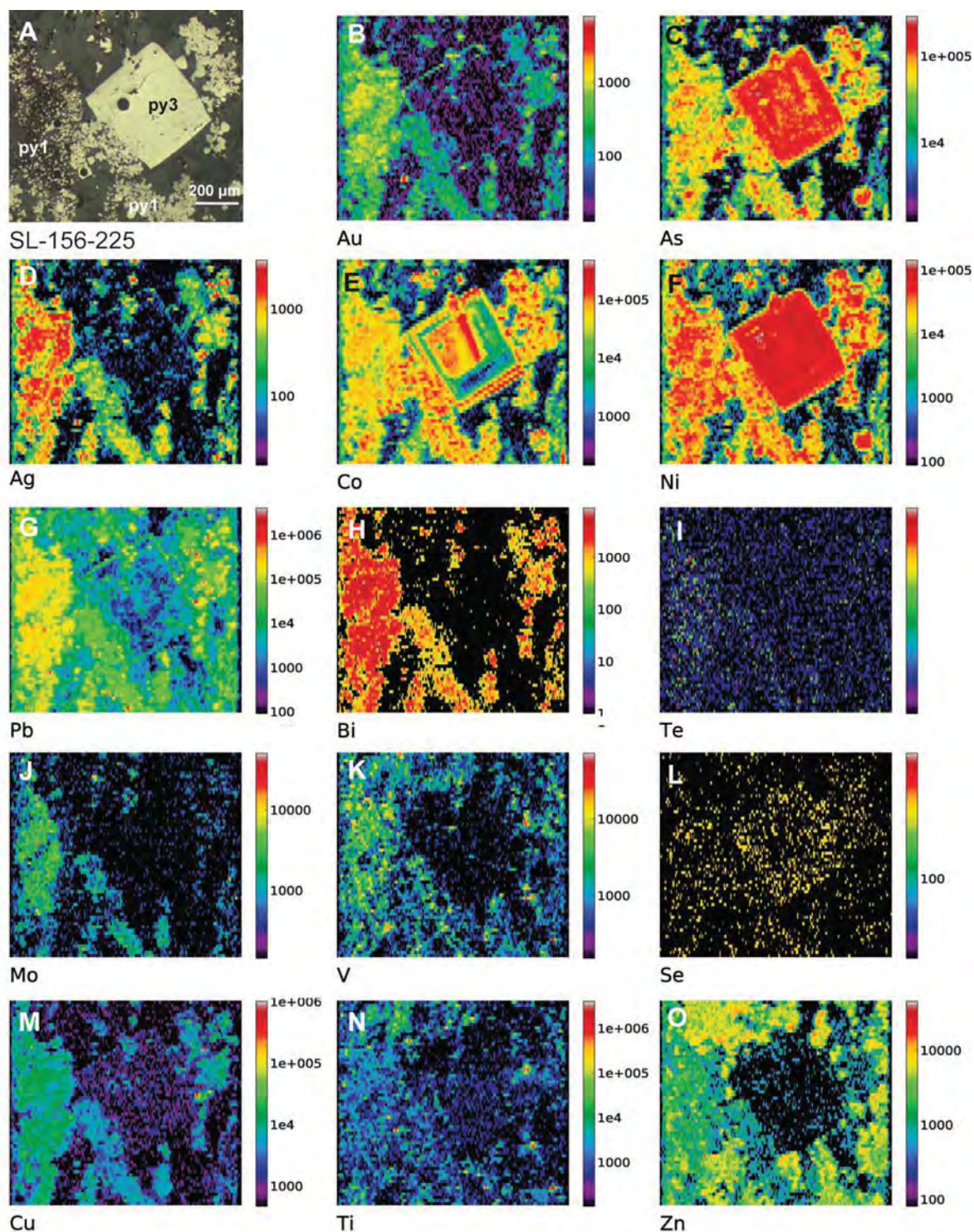
Fig. 3. LA-ICPMS images of trace elements in pyrite Sukhoi Log, sample SL-156-255. A. Fine framboidal diagenetic py1 and coarse euhedral early metamorphic py3. B. Au distribution in counts showing highest gold (warm colors, yellow and red) within the sooty framboidal pyrite. C. As distribution, showing highest arsenic (warm colors) in the py3 synmetamorphic cube, and lower As in the framboidal pyrite. D. Ag is enriched in the framboidal pyrite and lacking from the euhedral pyrite, except for a narrow rim. E. Co enriched in framboidal pyrite in both the core and thin outer rim of the euhedral py. F. Ni shows elevated counts in both the synmetamorhic euhedral py3 and syndiagenetic framboidal py1. G. H. J. M. Pb, Bi, Mo, and Cu are enriched in frambiodal pyrite. L. Minor Se enrichment in pyrite compared to sediment background, O. Zn is enriched in carbonate and Mg-bearing matrix but not in either type of pyrite. I, K, N. Very minor Te, V, and Ti enrichment in framboidal pyrite, but none in synmetamorphic euhedral pyrite.
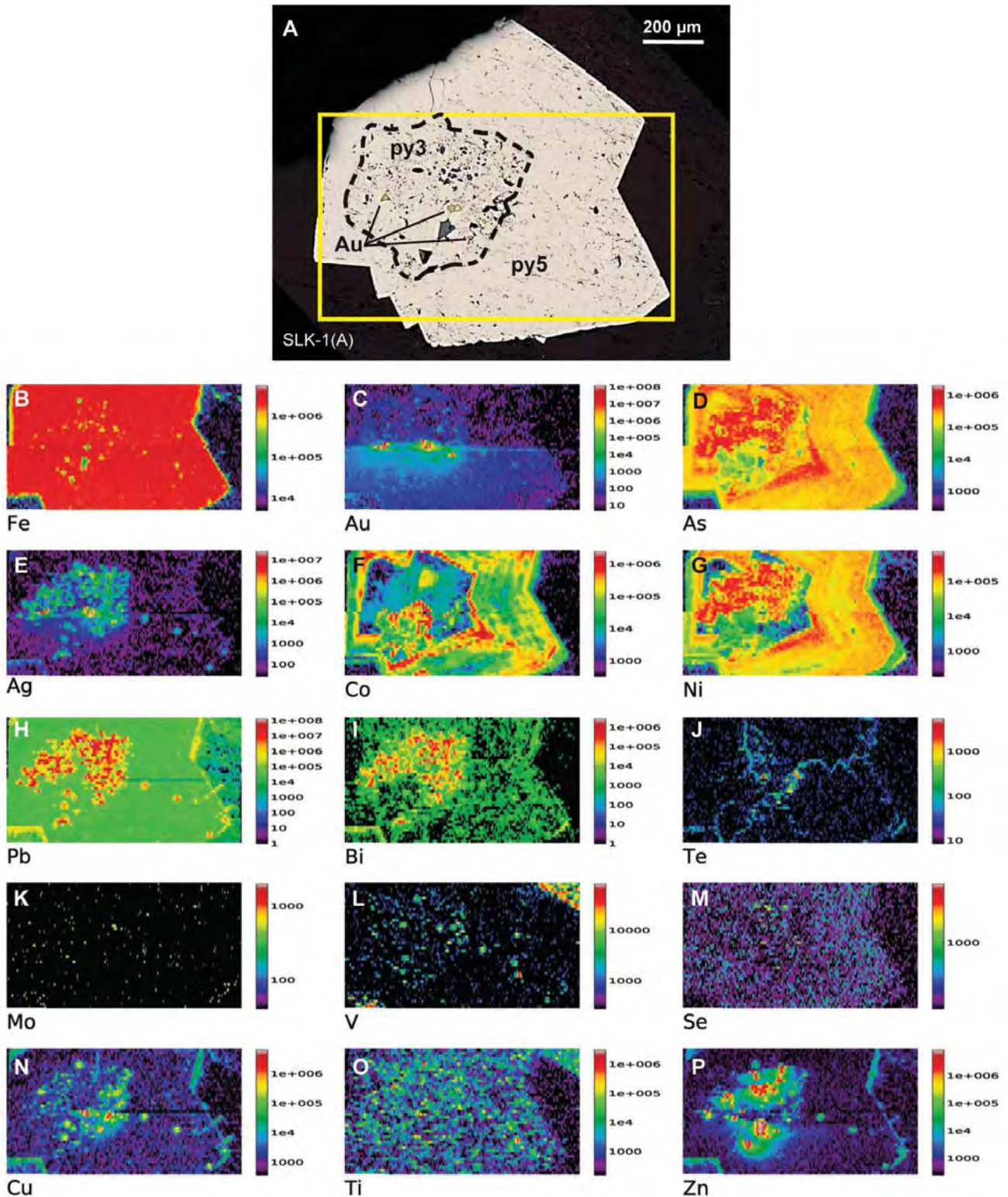
Fig. 4. LA-ICPMS images of trace elements in pyrite Sukhoi Log, sample SLK-1. Zoned pyrite aggregate in pyrite-quartz veinlet; late diagenetic to early metamorphic py3 core surrounded by late metamorphic and/or hydrothermal py5. The core contains inclusion of silicate matrix, chalcopyrite, sphalerite, galena, pyrrhotite, and native gold. Au image shows red-yellow spots in core due to inclusions of native gold. The light blue halo below the gold spots is due to gold splatter caused by the laser ablation process. The images show that the inclusion-rich pyrite core contains elevated As, Ag, Ni, Pb, Bi, Cu, and Zn. The euhedral metamorphic and/or hydrothermal overgrowth pyrite shows zoning of As, Ni, and Co.
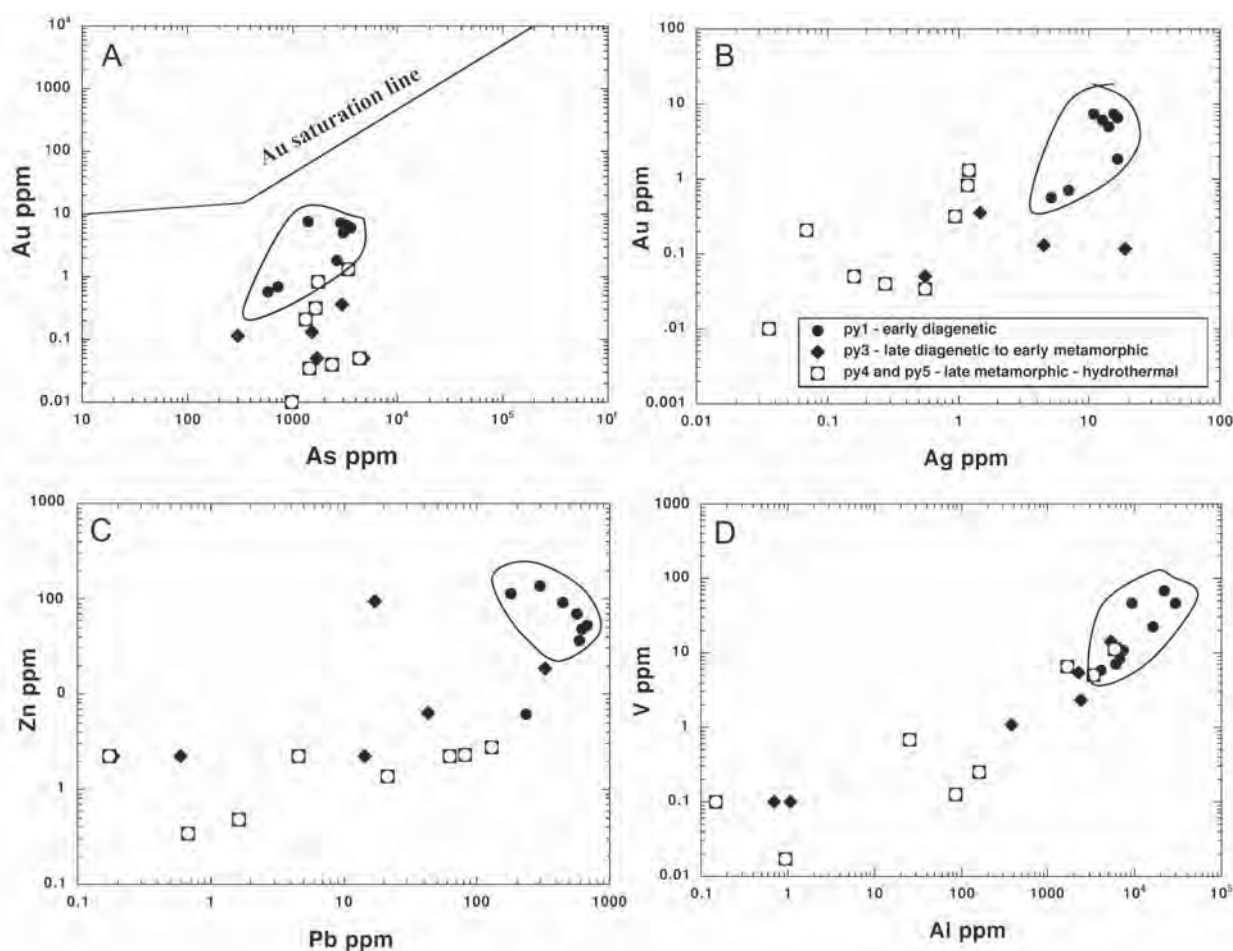
Fig. 5. Binary plots of selected trace elements in pyrite types from Sukhoi Log. The early diagenetic pyrite (outlined) has higher levels of Au, Ag, Pb, Zn, Al, and V compared with the later metamorphic and/or hydrothermal pyrite. The positive correlation between Al and V suggests that the V is present in Al silicate inclusions in the pyrite, rather than the pyrite structure.

Bendigo Pyrite

Gold in the Bendigo-Ballarat region of the Victorian gold province occurs principally in quartz vein saddle reefs developed in the hinge zones within a folded sequence of Devonian turbidites (Thomas, 1953; Cox et al., 1995; Willman, 2007). These ore deposits are classic examples of structurally controlled orogenic gold deposits (Groves et al., 1998; Ramsay et al., 1998), with recent research emphasizing that the ore fluids were derived from a deep-seated source, late during a period of protracted deformation (e.g., Phillips et al., 2003; Willman, 2007). Wood and Large (2007) favor an alternative model that involved gold enrichment in the sediments early during sedimentation, with later remobilization during deformation, to form the saddle reefs.

Pyrite types at Bendigo

Gold in the saddle reefs occurs as nuggety free gold, not commonly associated with pyrite. However previous workers (e.g., Li et al., 1998) describe the presence of gold-arsenic–bearing disseminated pyrite in the sediments surrounding the

saddle reefs. Our work has found disseminated pyrite, in the shale and sandstone units that host the saddle reefs, hundreds of meters away from the reefs. An important question to solve in this context is whether the gold-bearing pyrite in the host sediments is hydrothermal in origin or a mixture of both hydrothermal and diagenetic types. Resolution of this will help determine the timing of gold input into the basin.

Samples have been selected from several drill holes that intersected the Railway Shale, which is an interbedded shale, siltstone, and sandstone package that hosts the nearby Gill reef (Fig. 6), the current focus of mining activity. Pyrite in the sediments displays complex textures but can generally be grouped into two types: fine-grained pyrite, py1, which forms rounded or nodular clusters (0.2–1 mm across) of microcrystals (<10 μm; Fig. 7A-C), and coarser grained euhedral pyrite, py3, (0.5–5 mm), which may be internally zoned (Fig. 7D) or show composite intergrowth or overgrowth textures (Fig. 7E). In some pyrites, a third type of clear nodular pyrite, py2, occurs between py1 and py3 (Fig. 8A). The first pyrite in the paragenesis, py1, is interpreted as diagenetic and the common euhedral overgrowth, py3, as hydrothermal, developed
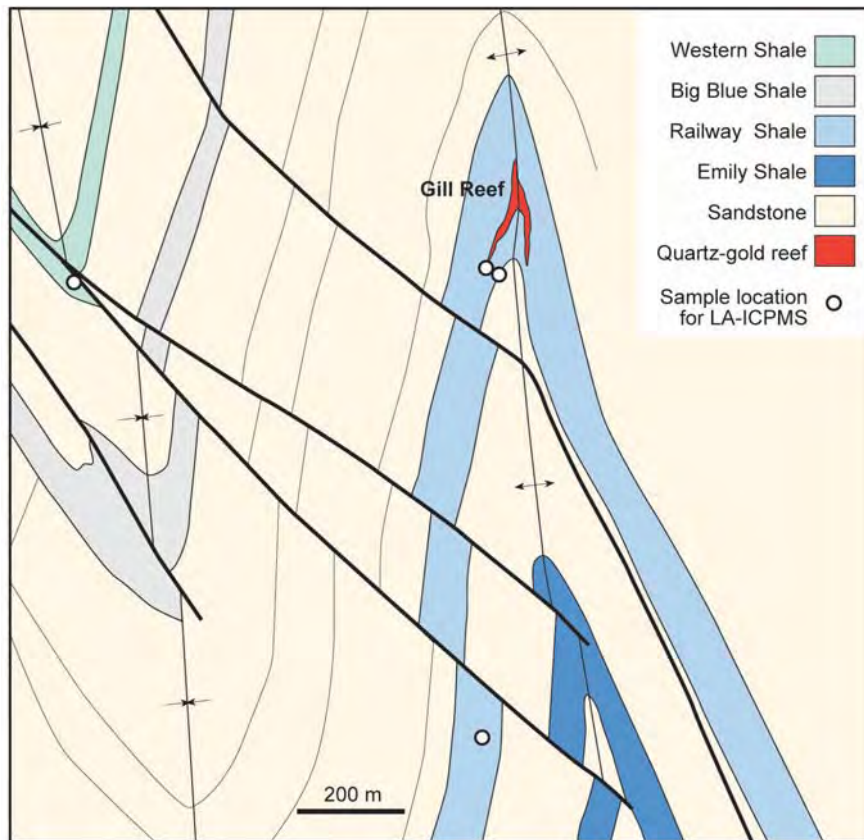
Fig. 6. Schematic geologic cross section of the Bendigo mine, Gill Reef, showing the major carbonaceous shale units and the locations of samples used in this study.

syn- to postmetamorphism and deformation (Table 2); although it is recognized that some original diagenetic pyrite may be recrystallized during metamorphism and assume the character of synmetamorphic or hydrothermal pyrite. The timing of py2 is not clear; it may be late diagenetic or early metamorphic.

Pyrite composition and zoning at Bendigo

Two pyrite aggregates in the sediments have been mapped by the LA-ICMPS imagining technique, including quantified spot analyses (Figs. 8–10). The first sample (NBD177-377) is of carbonaceous pyritic shale of the Western Shale in a synclinal position (Fig. 6). The second pyrite sample (NBD171-545.8) is hosted by a siltstone bed within the Railway shale 120 m downdip from the gold-bearing Gill reef (Fig. 6). The pyrite imaged in Figure 8A (NBD177-377) was selected for study as it displays, on acid etching, a composite overgrowth texture interpreted as diagenetic pyrite overgrown by hydrothermal pyrite. The core of the pyrite composite shows a sausage-shaped zone of porous py1 (1×0.1 mm), which may represent replacement of a worm tube or worm burrow (Fig 8A). This is surrounded by relatively clean (less inclusions), lenticular py2 (2×1 mm), with an oval-shaped concretionlike appearance. The outer edge of the py2 zone is marked by an irregular line of rutile inclusions along the boundary. The outer zone of pyrite (py3) in the composite has a euhedral shape and overgrows the inner py2. This outer zone py3 has an internal

fabric, similar to the deformation fabric in the surrounding shale matrix, indicating that py3 is hydrothermal in origin and replaced the sediment matrix during or postdeformation. It has a similar texture and paragenesis to py4 at Sukhoi Log (Large et al., 2007). A thin rim ($<70 \mu$m) is apparent on the outermost margins of the pyrite composite (Fig. 8A).

LA-ICMPS mapping (Fig. 9) and spot analyses (Fig. 8B, Table 1) highlight the complex zoning revealed by etching and shows that each zone has a different trace element chemistry. The sausage-shaped core of porous py1 contains elevated Ni (to 2,770 ppm), As (to 3,950 ppm), Cu (to 15,000 ppm), Mo (to 32 ppm), Ag (to 17 ppm), Te (to 12 ppm), Au (to 760 ppb), Pb (to 4,100 ppm), and Bi (to 105 ppm). The oval-shaped py2, surrounding the sausage-shaped core, contains elevated Ni but is low in Co and As. This zone also contains many microinclusions of Cu, Pb, Mo, Ag, and Bi, probably due to ultra small chalcopyrite and galena inclusions. The outer zone of hydrothermal py3 shows progressive zoning from an As-Co-Ni–rich inner zone, through a trace element depleted low As zone, to an outermost rim enriched in As (to 8,500 ppm) and Au (to 6,670 ppb). Detailed imaging (Fig. 8B) shows that the outer Au-As rim is actually composed of at least three separate rims, each about 20 μm thick. The Ti and V maps (Fig. 9K, N) highlight the rutile inclusions along the boundary between the oval pyrite core and hydrothermal overgrowth pyrite. Some As, but not Au, has penetrated along cracks in the py2 core (Fig. 9C), demonstrating that the
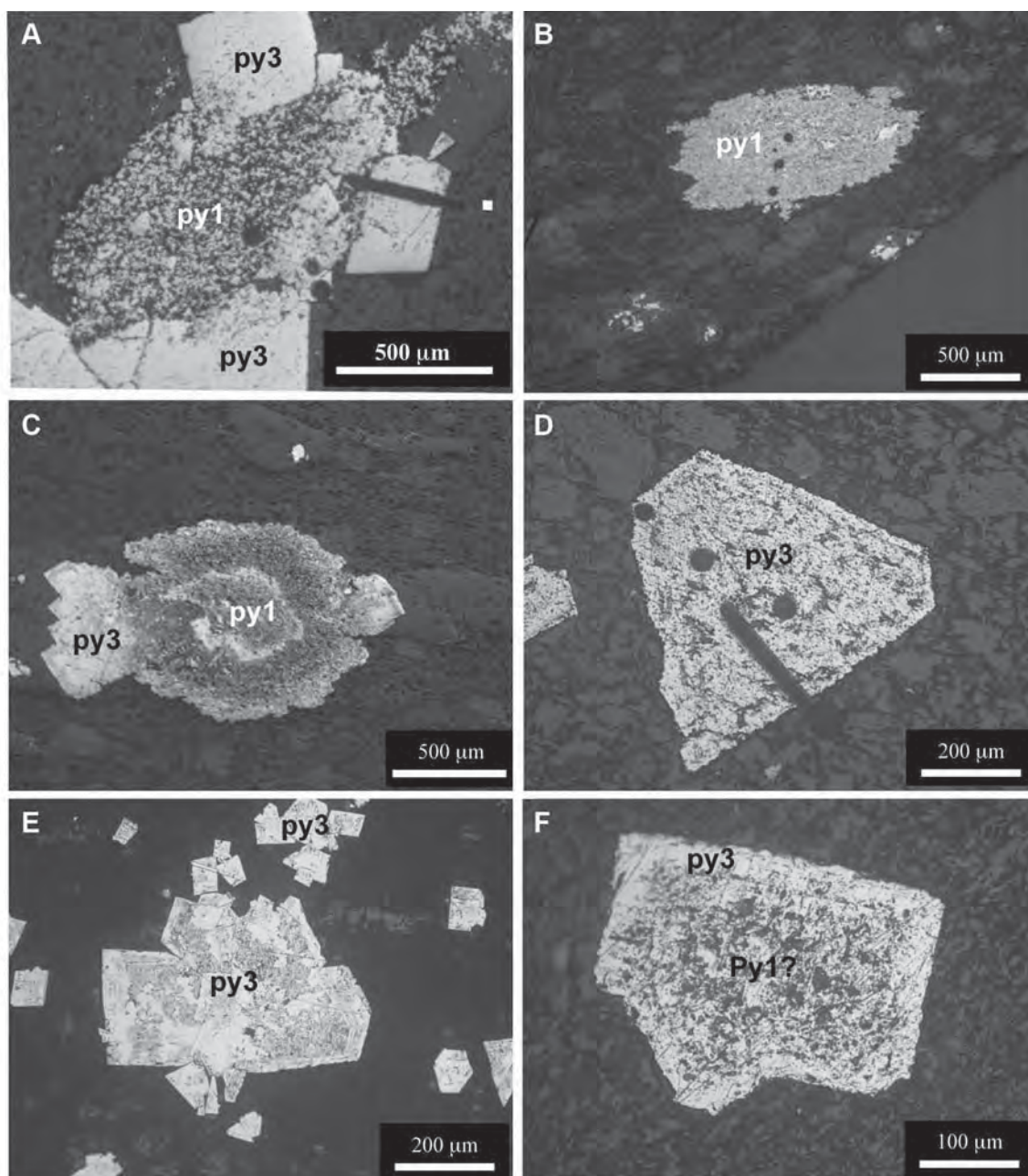
Fig. 7. Textures of pyrite types at Bendigo. A. Fine-grained diagenetic py1 partly overgrown by coarser euhedral syn-metamorphic hydrothermal py3. B. Fine-grained oval-shaped patch of diagenetic py1 after marcasite (?). C. Oval-shaped and zoned diagenetic py1, with euhedral metamorphic and/or hydrothermal py3 developed in pressure shadow. D.-F. Examples of porous euhedral metamorphic and/or hydrothermal py3, with poorly developed hydrothermal rims.

immediate zone of As-rich, but Au-poor, overgrowth py3 is later than the oval core py2. Note that Te (Fig. 9I) is concentrated in the inner core diagenetic py1 zone and also throughout the outer hydrothermal py3, whereas Se (Fig. 9L) is fairly evenly distributed through all pyrite types with no zonation. Gold in the inner core py1 is associated with elevated Ag, Te, As, Pb, Bi, and Mo, in contrast to gold on the outermost hydrothermal rim of py3, which is coincident with high As but no Te, Pb, or Mo.

The second pyrite sample (NBD171-545.8), selected from a siltstone bed, in the Railway Shale shows a different texture and metal zonation (Fig. 10). This pyrite grain is smaller than the previous (500 μm across compared to 3,000 μm) and exhibits an inner zone of inclusion-rich porous pyrite, surrounded by a euhedral rim of poorly zoned pyrite. This outer euhedral zone is less porous than the inner zone, suggesting that it is hydrothermal in origin (Table 2), however, the core zone of porous pyrite maybe either hydrothermal or diagenetic (Fig. 10A).
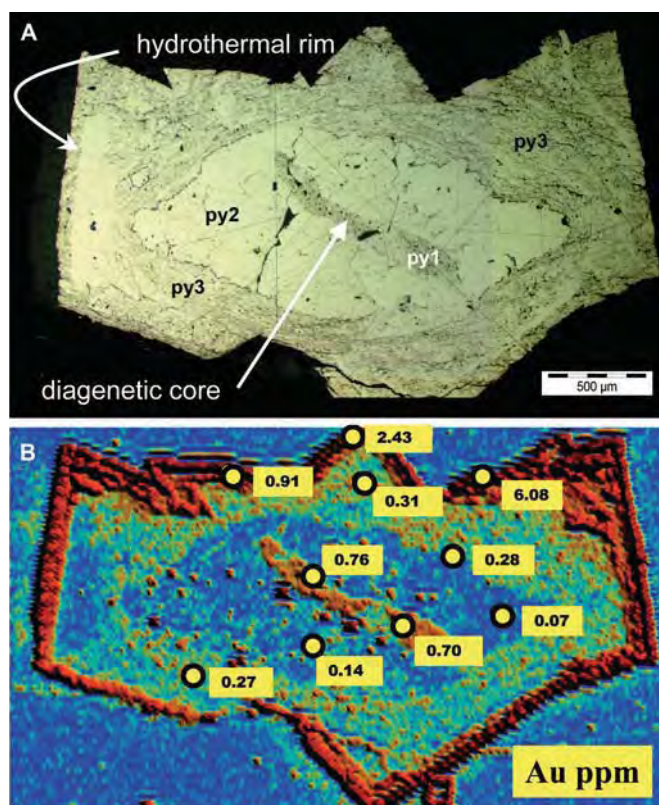
Fig. 8. A. Composite pyrite (sample NBD177-377) hosted by organic-rich black shale within the Western Shale, Bendigo mine. The pyrite has been etched with nitric acid to enhance the growth zones. B. Processed image of LA-ICPMS gold in the same pyrite composite, with digital enhancement using ER Mapper. Warm colors indicate higher gold content. Note the highest gold occurs on the outermost euhedral rim of py3, with lesser, but significant gold in the sausage-shaped porous py1 core. Note the gold-rich rim is revealed by the image enhancement to consist of three closely spaced and parallel microrims. Gold in the inner pyrite zones and the diagenetic py1 core has a spotty distribution, which correlates with the Pb, Bi, Te distribution (Fig. 9), suggesting the presence of invisible microinclusions of Pb-Bi-Au tellurides with the inner zone pyrite.

The LA-ICPMS map indicates progressive zonation of trace elements from core to rim of the pyrite. Pb and Ag are concentrated in the porous pyrite core, followed by elevated Bi-As-Co-Ni in the surrounding zone, and finally As-Au in the outermost euhedral rim. Gold is present at low to moderate levels (around 1–3 ppm) in the inner zones of the pyrite but is elevated (5–20 ppm Au) in the outermost 40-μm-thick As-Au rim (Fig. 10). Te, V, and Bi are at a maximum in the outer part of the pyrite core, where Au and As are slightly enriched.

Chemical distinction of pyrite types at Bendigo

The analyses of Bendigo pyrite listed in Table 1, determined on pyrite grains from five samples of sediments which host the gold reefs, have been plotted in Figure 11. The Au-As plot (Fig. 11A) shows that the data forms an elongate pattern with the outermost hydrothermal rim py3 at the Au-As–rich end of the trend. Diagenetic py1 in the core of sample 177-377 forms a cluster in the lower part of the Au-As trend.

Generally the diagenetic py1 at Bendigo is enriched in Ni, Cu, Mo, Ag, Bi, and Pb compared to the overgrowth and rim hydrothermal py3. In contrast the hydrothermal pyrites generally have lower trace elements but may be strongly enriched in Co in the innermost zone and show cyclic zonation of Co, Ni, and As. These patterns are somewhat similar to those recorded in Sukhoi Log pyrites (Table 3). Both diagenetic and hydrothermal pyrites at Bendigo contain elevated and spiky Bi and Te patterns, suggesting the presence of bismuth telluride microinclusions in the pyrite.

The chemical distinction between diagenetic py1 cores and the hydrothermal Au-As py3 rims are shown in Figure 11B-D. The elevated Pb and Mo clearly discriminate the diagenetic pyrite cores from the hydrothermal overgrowths in Figure 11C. In Figure 11D the positive Au-V trend of the pyrite core is distinguished from the negative Au-V trend in the Au-As hydrothermal rims.

Based on textures alone, it is not possible to determine whether the core of the pyrite in Figure 10 is of hydrothermal or diagenetic origin. The porous inclusion-rich nature, high Ag/Au ratio, and elevated Pb, Ni, V, and Te in the inner core support the interpretation of a diagenetic origin. Elevated Co and Bi in the outer part of the core zone suggest a hydrothermal origin. Thus the boundary between diagenetic and hydrothermal processes is tentatively suggested between the inner Pb-Ag-Te-V core and the outer Co-Bi zone (Fig. 10).

In both pyrite samples (Figs. 8–10) the main gold deposition event is the outermost pyrite rim, indicating that gold was concentrated at the final stages of deformation and hydrothermal pyrite growth. However in both cases, minor Au is also concentrated in the inner py1 core (with Ag-Pb-Bi-Te-Cu ± Mo), suggesting an early synsedimentary to diagenetic gold concentration event for Victorian orogenic gold deposits, as previously proposed by Wood and Large (2007).

Relationship of pyrite types and zonation to evolution of Bendigo

As with Sukhoi Log, the pyrite textures and trace element zonation suggest a multistage process in the formation of the Bendigo quartz-gold saddle reefs. Diagenetic pyrite aggregates (Fig. 7A-C) with enriched gold from 0.1 to 2 ppm (Fig. 11) occur in the most carbonaceous shale units in the host sediments at Bendigo. This early gold enrichment in the pyritic carbonaceous shales is accompanied by enrichment in As, Ni, Pb, Co, Cu, Mo, Ag, Sb, and Bi (Fig. 9, Table 3). The late diagenetic and early metamorphic and/or hydrothermal overgrowth pyrites contain only minor Au and As (Table 1), indicating that the initial fluids generated during folding carried little gold. However, these fluids were initially enriched in Ni and Co with minor Bi and Te (Fig. 9E-F, H-I). The strong Au and As enrichment on the outermost rim of the hydrothermal pyrites (Figs. 8–10) indicates a climax in gold-arsenic transport and deposition late during deformation-related fluid flow in agreement with previous workers (Schaubs and Wilson, 2002; Willman, 2007). This late Au-As event is accompanied by minor Ni but relatively low levels of Ag, Co, Pb, Bi, Te, Mo, and Cu compared to the early diagenetic gold event. The enhanced gold-pyrite image in Figure 8B indicates at least three pulses of gold enrichment on the hydrothermal pyrite rim. These pulses may relate to fold lock-up

TABLE 2. Textural and Chemical Criteria to Assist in the Distinction between Diagenetic and Metamorphic and/or Hydrothermal Pyrites in Sediment-Hosted Gold Deposits[1]

Criteria	Early diagenetic pyrite (Bendigo, Spanish Mountain, Sukhoi Log, and Carlin Trend0	Hydrothermal pyrite (Bendigo, Spanish Mountain, and Sukhoi Log)	Hydrothermal pyrite (Carlin Trend main stage)
Texture: Size and shape	Fine-grained ($<5 \mu$m), stratiform, clusters of microeuhedral crystals ($50–150 \mu$m), framboidal, sooty or microneedles (after marcasite); rounded shapes are common	Coarse-grained (0.5–50 mm), strata bound or crosscutting, euhedral with cubic shape, may be zoned	Fine-grained; rims ($2–20 \mu$m) on preexisting pyrite, cubic, or needle shapes, porous spongy aggregates
Texture: Internal	Abundant inclusions of sediment matrix material randomly oriented	Commonly clear, inclusion-free; etching with HNO_3 may reveal deformation fabric of sedimentary host rock replaced by pyrite	Abundant inclusions; etching with HNO_3 gives brownish coloration due to high As content
Composition of pyrite: General	Abundant trace elements; commonly, but not always, As, Ag, Ni, V, Pb, Mn, Zn, Cu, Mo, Se, Te	Low levels of most trace elements, except As, Co, Ni, Se	Enriched in As, Sb, Tl, Cu, Hg, Ag, Pb
Outermost pyrite rims	Rarely present	Two types of rims: Au-As–rich in high-grade ores; Co-Ni–rich in low-grade ores	High enrichment in Au and As
Silver	1 < Ag < 400 ppm	0.01 < Ag < 10 ppm	50 < Ag < 1,000 ppm
Vanadium	3 < V < 10,000 ppm	0.01 < V < 60 ppm	0.1 < V < 60 ppm
Nickel	100 ppm < Ni < 2 wt %	5 < Ni < 1,000 ppm	5 < Ni < 100 ppm
Zinc	2 < Zn < 5,000 ppm	0.1 < Zn < 20 ppm	0.1 < Zn < 30 ppm
Molybdenum	0.4 < Mo < 3,000 ppm	0.01 < Mo < 4 ppm	4 < Mo < 150 ppm
Selenium	2 < Se < 5,000 ppm	2 < Se < 140 ppm	4 < Se < 220 ppm
Manganese	1 < Mn < 3,000 ppm	0.1 < Mn < 50 ppm	0.5 < Mn < 60 ppm
Arsenic	400 < As < 7,000 ppm	60 ppm < As < 1.6 wt %	1 wt % < As < 10 wt %
Gold	0.01 < Au < 200 ppm	0.01 < Au < 30 ppm	50 < Au < 2,000 ppm

[1] Based on data in this study from Bendigo, Spanish Mountain, Sukhoi Log, and northern Carlin Trend

and fault-enhanched fluid flow toward the end of deformation (e.g., Willman, 2007).

Spanish Mountain Pyrite

Spanish Mountain is a large gold resource hosted in Upper Triassic black shales and graywackes at the base of the Quesnel trough, a continental margin sequence in central British Columbia (Panteleyev et al., 1996). Recent drilling by Skygold has defined a zone of disseminated pyrite, carbonate alteration, and minor quartz veining within a strongly deformed sequence of shales, phyllites, and meta-volcaniclastics (Fig. 12). A measured plus indicated resource of 102 Mt at 0.8 g/t Au was released by the company in 2009. In this study we investigated pyrite textures and geochemistry from one drill hole (DDH-252, Fig. 12) passing through the main mineralized zone.

Spanish Mountain geology consists of shale, siltstone, and graywacke sequences with minor intrusive and volcanic facies. These units are generally interbedded, folded, thrust "stacked," or repeated. The dominant structural features are isoclinal to recumbent folding and open large-scale warping and extension, with associated faulting and veining. Alteration consists primarily of ubiquitous iron carbonate and sericitization with local silicification and albitization. The widespread disseminated low-grade gold-pyrite mineralization is generally strata bound, being hosted in carbonaceous shale, siltstone, and graywacke sequences; for example, hole 06-DDH-252 (Fig. 12), from which samples for this study were taken, intersected 109.5 m of 1.20 g/t gold.

Pyrite types at Spanish Mountain

Pyrite in the carbonaceous shales and phyllites in DDH 252 through the center of the mineralized strata, typically occurs in euhedral cubic crystals from about 1 mm to 1 cm across, as isolated euhedra, clusters of euhedral crystals, or bands of euhedral crystals. Quartz pressure shadows and coarse euhedral form indicates that most of the pyrite grew (or recrystallized) during deformation. Some pyrite bands are folded, others crosscut the bedding and metamorphic fabric. Quartz veins cut the pyrite bands and occur later. These relationships suggest multiple growth phases of pyrite from diagenetic to hydrothermal, all cut by late-stage quartz veining.

Under the microscope, pyrite textures are complex and suggest three main stages of pyrite growth (Fig. 13). Py1 in the cores of pyrite aggregates form irregular anhedral rounded or elongate shapes. These textures suggest corrosion of py1 before the deposition of py2. Py2 contains abundant dark inclusions of matrix and organic matter(?) and displays a subhedral outline. Py3 overgrows py2, with a strong euhedral shape and clear pyrite texture with minimal inclusions. Based on these textural relationships py1 is interpreted to have grown during diagenesis and py3 is a hydrothermal pyrite that
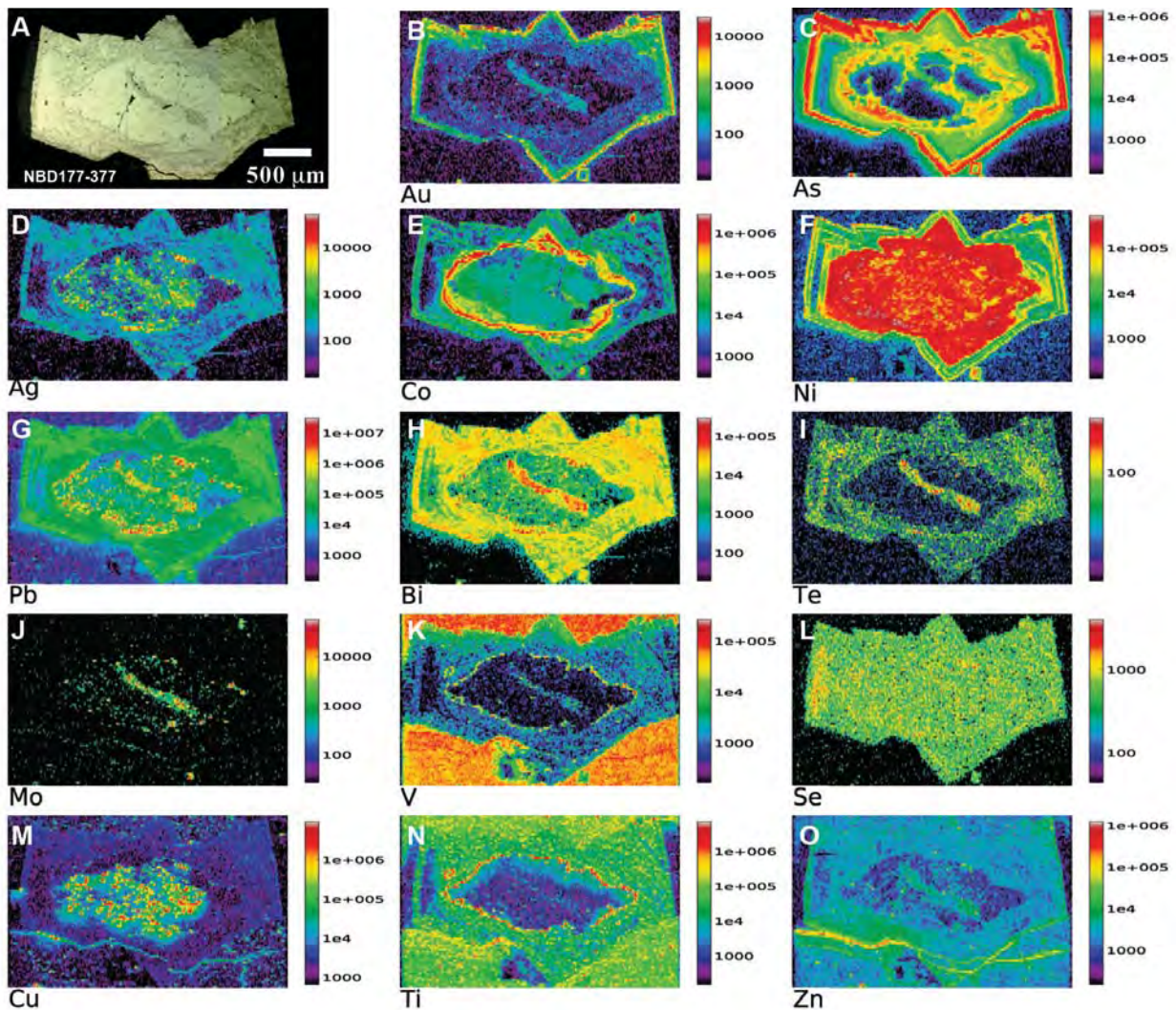
Fig. 9. LA-ICPMS images of trace elements in Bendigo pyrite, sample NBD177-377 (see Fig. 6 for details of pyrite texture). The sausage-shaped diagenetic py1 core is enriched in Au, As, Ag, Pb, Bi, Te, Mo, V, and Zn compared with the surrounding oval-shaped py2 zone. Py2 contains microinclusions enriched in Pb, Ag, and Cu. The outermost euhedral py3 zone has a rim enriched in Au and As. Note Ti and V are concentrated in a narrow zone of rutile inclusions developed between py2 and py3.

formed during metamorphism. Py2 may have developed late during diagenesis, as indicated by the abundant inclusions, or early during metamorphism, as suggested by the euhedral outline. The boundary between py1 and py2 (Figs. 11A, 13B-C) is marked by inclusions of rutile, similar to those observed in some Bendigo pyrites (Fig. 8). Minor grains of free gold were observed in py3 in some samples.

Pyrite composition and zoning at Spanish Mountain

Trace element LA-ICPMS images and spot analyses (Figs. 14–16) of gold-bearing composite pyrites in sample SM1-79.8 from DDH 252 commonly exhibit all three zones (py1, py2, and py3). The imaging shows that the diagenetic py1 cores are generally enriched in Ni, Zn, As, Ag, Au, and Pb compared to the outer hydrothermal py3. The latter shows a gradual decrease in As toward the pyrite rim, with two zones of elevated Co and Ni, one on the inner margin and the other

on the outer rim. Py2 in Figure 14 is too narrow to interpret the chemistry. The boundary between py1 and py2 is marked by elevated Ti and V, due to inclusions of rutile. Quantitative LA-ICPMS spot analyses of the same pyrite (Fig. 15, Table 1) indicate that the diagenetic cores contain consistently elevated Au, As, and Ni, up to 19,570 ppb Au, 15,900 ppm As, and 2,900 ppm Ni. The hydrothermal py3, by comparison, has much lower values of these elements (up to 170 ppb Au, 5,570 ppm As, and 670 ppm Ni). Similar patterns are evident in another complex pyrite composite from Spanish Mountain (Fig. 15B). This sample shows a thick zone of py2, which has intermediate gold values between those of py1 and py3. The uniform nature of the gold image in Figure 14B and the consistent values in the spot analyses suggest that gold in the diagenetic cores may be present as gold dissolved in the arsenian pyrite structure, however, further analysis by high-resolution transmission electron microscopy (e.g., Deditius et
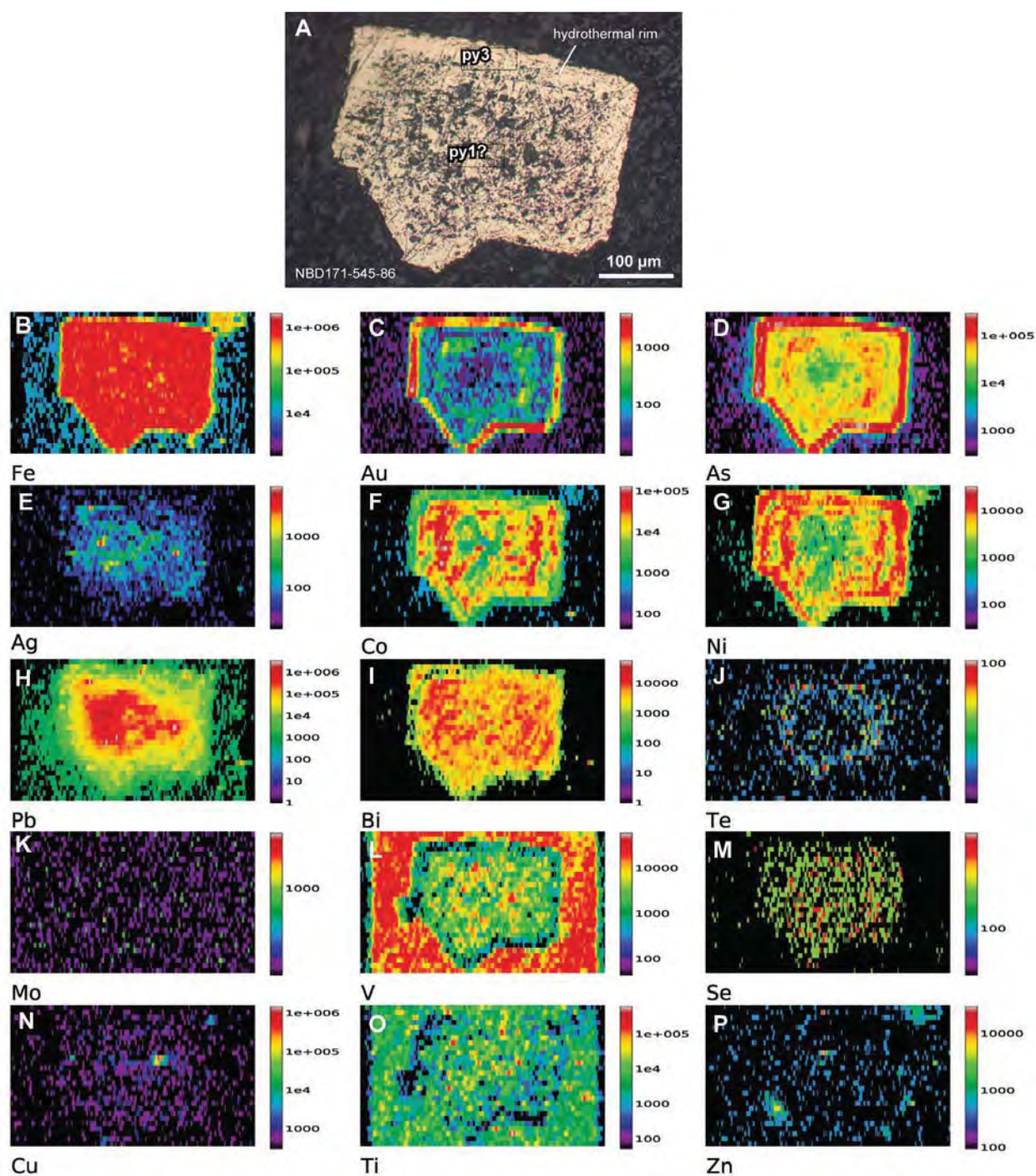
Fig. 10. LA-ICPMS trace element images of pyrite (NBD 172-545.8) from a sandstone unit in the Railway Shale, Bendigo mine. This pyrite contains a porous core of possible (?) diagenetic origin, surrounded by a 35-μm-thick pyrite rim of metamorphic and/or hydrothermal origin. The LA-ICPMS maps show zonation of various elements from the core to rim. The pyrite core is enriched in Pb and Ag. In contrast the outermost metamorphic and/or hydrothermal rim is enriched in Au and As. A transition zone between the core and rim shows enrichment in Bi, Te, Au, Co, and Ni.

al., 2009) is required to verify this interpretation. The spotty Pb (Fig. 14E) and Zn images, on the other hand, indicate submicroscopic inclusions of galena and sphalerite in the core zone. One grain of free gold has been imaged (Fig. 13B) on the right-hand side of the sample near the edge of the hydrothermal py3. This may be free gold liberated from the recrystallization of py1 containing invisible gold.

A second pyrite map from the same sample (SM1-79.8) is shown in Figure 16. This map shows an Au-As-Ni–rich core of porous inclusion-rich pyrite, surrounded by cyclic Co-Ni
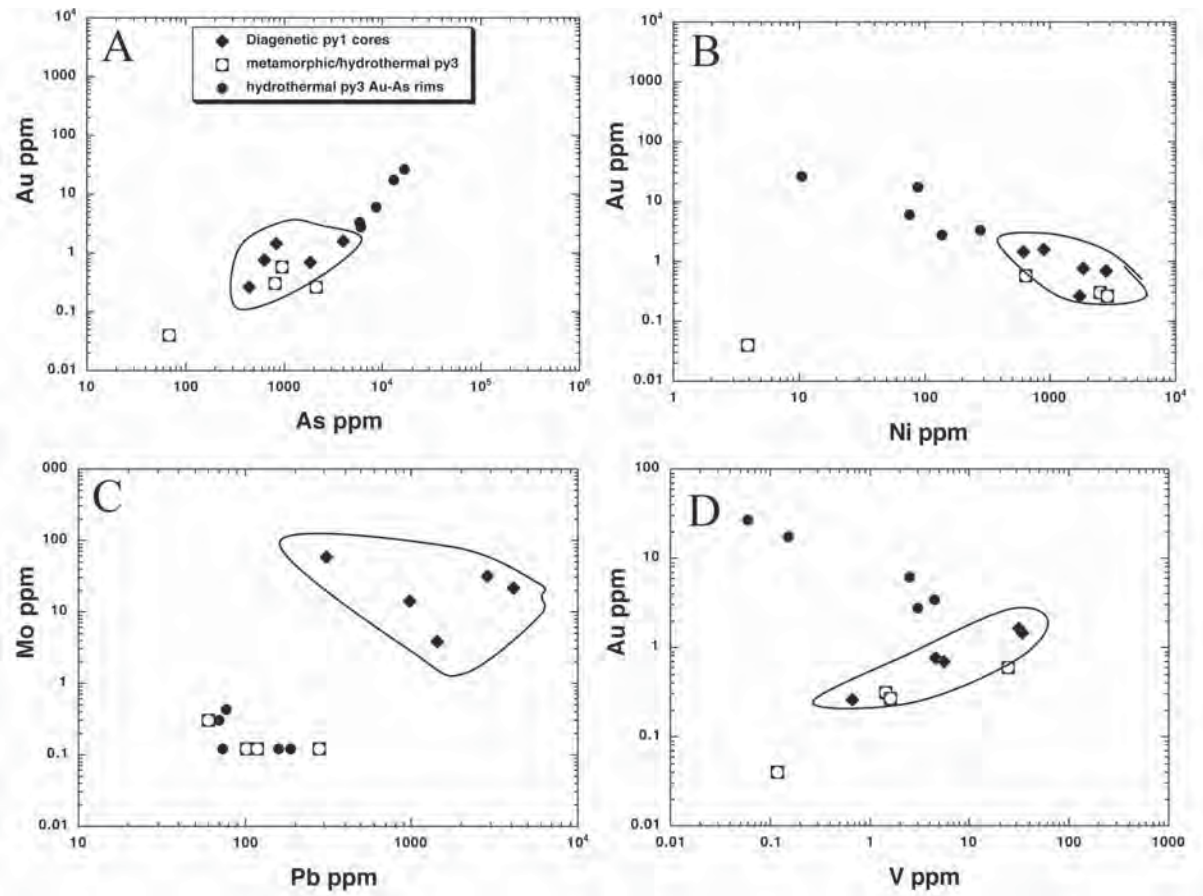
Fig. 11. Binary plots of selected trace elements in pyrite types from Bendigo. Diagenetic py1 group (outlined) generally has higher levels of Ni, Mo, and Pb, but lower As and Au, than the hydrothermal py3 rims. Pb and Mo show the best discrimination between the diagenetic and hydrothermal groups.

zones, with a general decrease in As to the outermost euhedral hydrothermal pyrite rim. As with the previous pyrite map, the core is strongly enriched in gold, plus inclusions of Cu (chalcopyrite), Zn (sphalerite), and Pb-Ag (galena). The early Au-rich pyrite core is totally devoid of Co. By contrast the hydrothermal overgrowth pyrite is Co bearing (Fig. 16).

Chemical distinction of Spanish Mountain pyrite types

The LA-ICPMS maps (Figs. 14, 16) and the spot analysis data from Table 1, plotted in Figure 17, show that the pyrite cores (py1) in the Spanish Mountain deposit are generally enriched in Au, As, Ag, Ni, Pb, and Zn compared to the later euhedral synmetamorphic hydrothermal pyrite overgrowths. The trace element composition of the cores support our previous interpretation, based on textures, that they are diagenetic in origin (Table 2). The pyrite zone (py2) developed between the py1 core and py3 hydrothermal rim shows intermediate trace element values (Fig. 17).

These pyrite trace element patterns show some similarity to those recorded at Sukhoi Log and Bendigo (Table 3), except that the early pyrite at Spanish Mountain shows no enrichment in Mo, Se, or V. Unlike Bendigo, but similar to Sukhoi Log, the Spanish Mountain pyrite shows no As-Au–enriched hydrothermal rims.

TABLE 3. Summary of Enriched Trace Elements (>100 ppm) in Major Pyrite Types at Sukhoi Log, Spanish Mountain, Bendigo, and Northern Carlin Trend (elements in order from maximum to minimum)

Deposits	Trace elements enriched in diagenetic pyrite (>100 ppm)	Trace elements enriched in metamorphic and /or hydrothermal pyrite (>100 ppm)	Trace elements enriched in outermost pyrite rim (>100 ppm)
Sukhoi Log	As, Ni, Mn, Pb, Co, Ti, Cu, Zn	As, Ni, ±Co	Ni, ±Co
Spanish Mountain	As, Ni, Cu, Pb, Se, Ti	As, Ni, Se, ±Co	Ni, Co
Northern Carlin Trend	Cu, As, Ni, Se, V, Mo, Sb, Mn, Pb, Tl, Ag, Ti	As, Sb, Tl, Cu, ±Ag, Pb	As, Au, Cu, Sb, Tl, ±Pb, Ag
Bendigo	As, Ni, Pb, Co, Ti, Cu, Sb, Bi	As, Ni, ±Co, Pb, Sb	As, Pb, minor Au
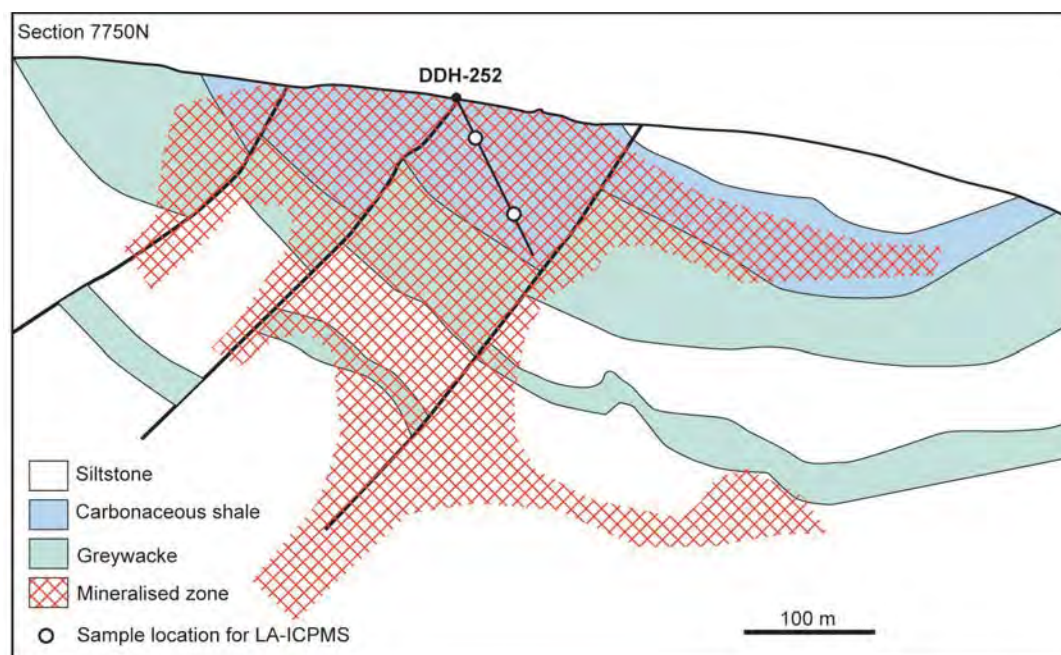
Fig. 12. Schematic geologic cross section of Spanish Mountain gold deposit, showing the major carbonaceous shale unit and the locations of samples from drill hole 252.

Relationship of pyrite types and zonation to evolution of the Spanish Mountain deposit

Only a small number of samples have been studied from one drill hole at Spanish Mountain, and thus it is not possible to draw any definitive conclusions from the pyrite textures and composition concerning the evolution of the deposit. Based on our samples, the main gold enrichment appears early, associated with As, Ni, Cu, Pb, and Se within corroded pyrite grains interpreted as diagenetic, within the carbonaceous shales. Invisible gold up to 20 ppm, As up to 1.6 wt percent, and Ni up to 3,100 ppm have been measured in the diagenetic pyrite cores. The synmetamorphic overgrowth euhedral hydrothermal pyrite is As rich (4,000–6,000 ppm), contains much lower invisible gold (<1 ppm), but has minor free gold along cracks in the pyrite. The hydrothermal pyrite has no rims enriched in Au or As. This may be interpreted to indicate that the hydrothermal event has remobilized gold from earlier pyrite generations but has not introduced new gold from an external source.

Carlin Pyrite

The Carlin deposits of Nevada contain over 50 Moz of gold, contained in over 40 separate deposits (Teal and Jackson, 1997). The gold is refractory, occurring as invisible gold in fine-grained arsenian pyrite (Bakken et al., 1989; Fleet et al., 1989), hosted in a Siluro-Devonian continental margin sequence of carbonaceous mudstones and silty limestones. The main gold mineralization event was in the Tertiary between 42 and 36 Ma associated with basin inversion (Cline et al., 2005). Emsbo et al. (1997, 1999) have also recognized a syngenetic gold event in the Devonian at the Rodeo and Meikle deposits. The origin of the gold ore fluids has not been resolved, with magmatic, metamorphic and meteoric fluids being proposed by different researchers (Cline et al., 2005).

Pyrite types in Carlin deposits

Gold-bearing pyrite in the Carlin deposits is arsenic rich, very fine grained, and commonly comprises only 4 to 10 wt percent of the carbonaceous sedimentary host rock. There are several generations of pyrite in the Carlin deposits, which have been described in detail by previous workers (e.g., Wells and Mullins, 1973; Hofstra and Cline, 2000; Kesler et al., 2003; Scott et al., in press). Scott et al. (in press) outlines criteria for the interpretation of pyrite timing based on relationships to (1) soft-sediment deformation, (2) early sulfate diagenetic nodules, and (3) widespread hydocarbon veinlets. On this basis they classify the pyrite as (1) syngenetic to very early diagenetic, (2) early diagenetic, and (3) late diagenetic to hydrothermal. The early diagenetic pyrite (Fig. 18A-D) typically occurs as very fine grained clusters of microcrystals aligned parallel to bedding to form elongate patches (0.1–5 mm long), in some cases (Fig. 18A) affected by soft-sediment deformation. In contrast the pyrite related to the main Tertiary gold event occurs as discrete, very fine grained anhedral or needle-shaped grains (after marcasite), thin pyrite rims (commonly 2–20 μm thick) on preexisting pyrite (Fig. 18E) or porous spongy aggregates (Fig. 18F).

The pyrite samples mapped by LA-ICPMS for this study were specifically selected to enable a comparison of the composition and zonation of pyrite from the Devonian sedex gold horizon defined by Emsbo et al. (1997), with pyrite from typical Tertiary gold mineralization of main-stage Carlin type.

Pyrite composition and zoning in Carlin deposits

We have undertaken over a thousand LA-ICPMS analyses of pyrite from the northern Carlin Trend as part of another study (Scott et al., 2008). For this study, we report representative LA-ICPMS analyses of two pyrite types (Table 1):
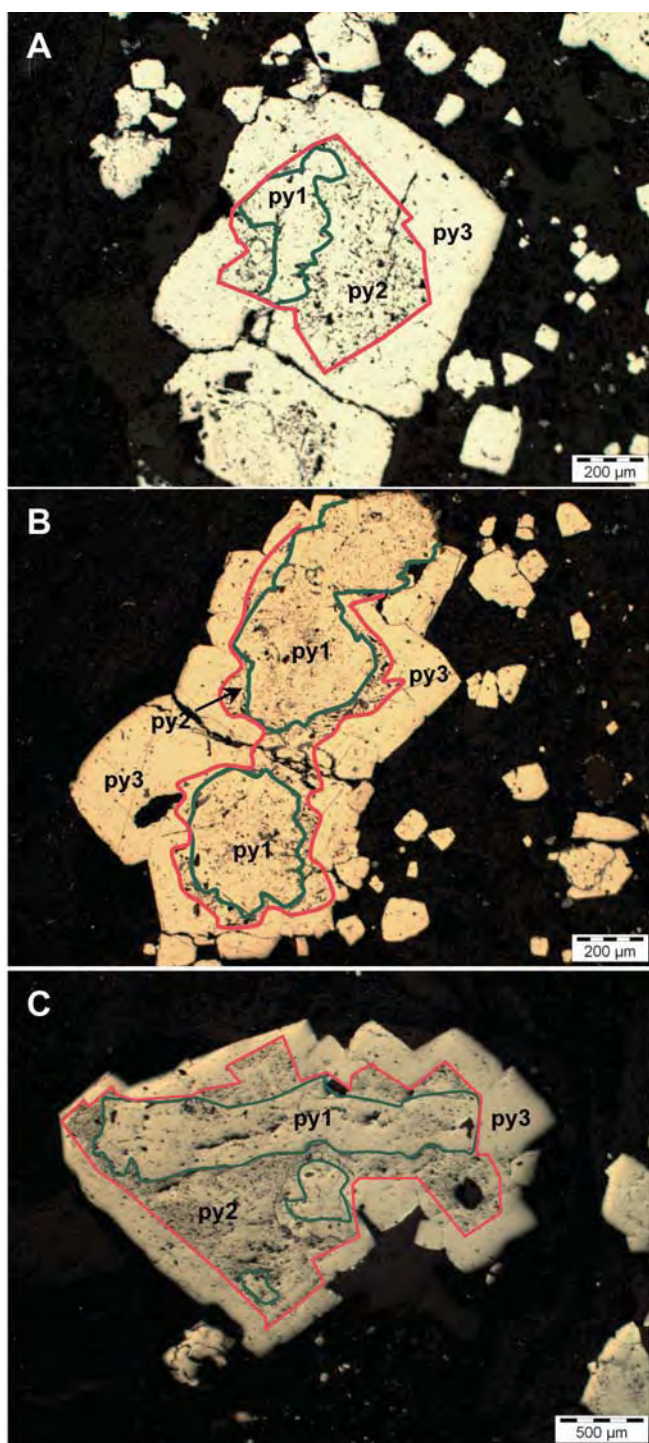
Fig. 13. Textures of pyrite types at Spanish Mountain. Irregular-shaped diagenetic core (py1) is outlined in green. Surrounding inclusion-rich pyrite (py2) is outlined in red. Euhedral, clear metamorphic and/or hydrothermal pyrite (py3) forms the outermost zone.

gold-bearing diagenetic (sedex) pyrite in strongly carbonaceous mudstones in two samples (R11-156M-4-224 and R11-156M-4-225) from a drill hole within the Rodeo deposit, and gold-bearing main-stage pyrite rims and porous aggregates

related to the Tertiary mineralization from Gold Quarry (sample QC 1489-890.5) and Meikel (samples M-DOL and M-EX92-904).

Only a small percentage of diagenetic pyrite in the Carlin district is gold bearing, and most of this comes from the organic-rich metalliferous horizon in the Upper Mud Member of the Popovich Formation (Scott et al., in press). Previous analyses by Emsbo et al. (1997, 1999) showed that the Devonian sedex gold mineralization is enriched in Zn, Pb, Cu, Ag, and Sb, compared to the Carlin Tertiary gold mineralization, which has higher levels of As, Tl, W, and Te. Our data in Tables 1 to 3 and Figures 19 and 20 confirms these patterns and shows the importance of some other critical elements.

Figure 19 is an LA-ICPMS image of a cluster of diagenetic pyrite microcrystals in an unaltered organic-rich mudstone in the Upper Mud Member of the Popovich Formation from the Rodeo deposit (sample R11-156-4-255). The whole-rock sample interval analyzed 28 ppm Au and 215 ppm As and showed none of the alteration typically associated with Carlin main-stage mineralization, such as decarbonatization, argillization, or silicification (Cline et al., 2005). The pyrite cluster in Figure 19 is only 300 μm long and 60 μm wide. The image shows that the diagenetic pyrite is strongly enriched in Ni, Cu, As, Se, Mo, Ag, Te, Au, and Pb compared with the sediment matrix. From the analyses shown in Table 1 and Figure 18, it is apparent that the trace metal content of the diagenetic pyrite in the metalliferous horizon at Rodeo varies from 10 to 322 ppm Au, 2,085 to 6,575 ppm As, 113 to 343 ppm Ag, 133 to 3,410 ppm Zn, and 266 to 577 ppm Pb. Also of interest are the very high levels of Ni (1,170–9,600 ppm), Se (2,735–4,250 ppm), Mo (450–2,660 ppm), and V (860–4,540 ppm) in the diagenetic pyrite. These latter four elements form strong organometallic bonds and are indicative of enrichment by organic processes during diagenesis (e.g.,Wood, 1996; Coveney, 2000).

Figure 20 is an LA-ICPMS image of porous pyrite related to the main-stage Tertiary Carlin mineralization at Gold Quarry in the northern Carlin Trend. The sample comes from drill hole QRC 1489 at 271.5 m in the mineralized Roberts Mountain Formation at Gold Quarry. The core interval that contained this sample varied from 7 to 10 ppm Au. The multielement image in Figure 20 shows that the porous pyrite has a complex metal-zoned "lacy" texture surrounding small-zoned subhedral pyrite cores. The small pyrite cores are zoned Co-Ni-Pb from center to rim. These are surrounded by the spongy main-stage Carlin pyrite, which is complexly enriched in Au-As-Cu-Pb-Ag to give the lacy texture. Quantified spot analyses of this and other Carlin main-stage rim pyrite (Table 1) indicates gold from 50 to 1,860 ppm and arsenic from 1.5 to 7.4 wt percent. The lacy nature of the Au and As distribution in Figure 20C and D indicates that the high gold and arsenic is not evenly distributed through the spongy pyrite but occurs as very thin rims on the spongy pyrite (e.g., Kesler et al., 2003). Copper, Te, Tl, and W are also generally elevated in the spongy pyrite, but other elements (particularly Ni, Zn, Se, Mo, and V) are commonly well below the levels found in the diagenetic pyrite of the metalliferous horizon at Rodeo.

Chemical distinction of Carlin pyrite types

Scott et al. (in press) provides a detailed discussion on the trace element differences between early syngenetic and/or
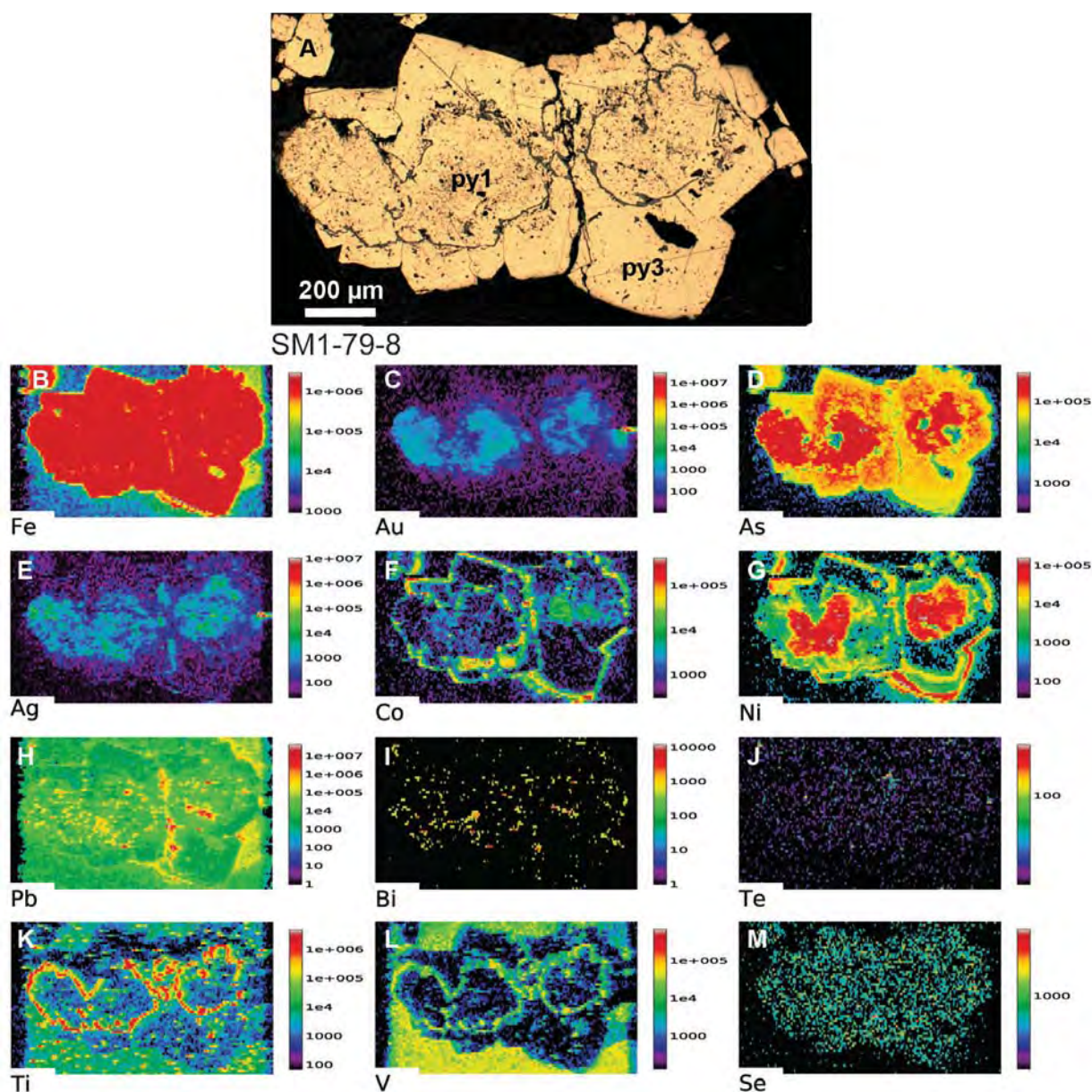
Fig. 14. LA-ICPMS images of trace elements in a composite pyrite aggregate from Spanish Mountain, sample SM-78.9. More detailed textural relationships are shown in Figure 10A. The rounded diagenetic pyrite cores contain uniformly elevated Ni, As, Au, and Ag, suggesting that these elements may be either dissolved in the pyrite structure or present as nanoparticles. Pb shows a spikey distribution due to microinclusions of galena in the cores. The outer metamorphic and/or hydrothermal pyrite zone contains uniformly elevated As but no Au. Ti and V are enriched in rutile inclusions, which form a narrow ring around the pyrite cores and along a central crack (Fig. 11H). The thin outermost rim on the metamorphic and/or hydrothermal pyrite is enriched in Ni and Co, but depleted in As, compared with the outer zone pyrite generally.

diagenetic pyrite in the Upper Mud Member of the Popovich Formation and later hydrothermal main-stage gold-enriched pyrite of Tertiary age, and only a brief summary is given here. The main chemical feature of the diagenetic gold-bearing pyrite in the metalliferous horizon at Rodeo is the very high levels of Ni, Se, Mo, and V, all greater than 500 ppm and commonly over 1,000 ppm. Chromium and Zn are also enriched over 1,000 ppm in some diagenetic pyrites. In contrast the main-stage Tertiary Carlin pyrite is strongly enriched in As

and Au, with lesser enrichment in Cu, Sb, Pb, Ag, Te, Tl, and Bi but showing a lack of significant Ni, Se, Mo, and V (Tables 1, 3, Fig. 21).

Relationship of pyrite types and zonation to evolution of Carlin deposits

The pyrite textures and chemical zonation revealed by this study support the previous work of Emsbo et al. (1997, 1999), which demonstrated an early phase of synsedimentary gold
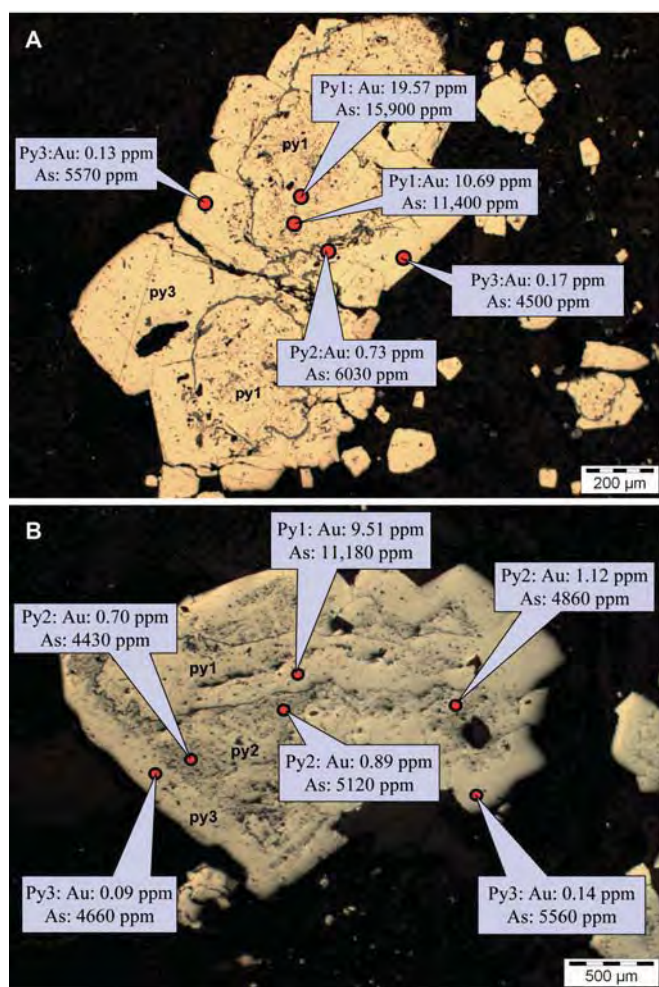
Fig 15. Spot LA-ICPMS analyses of selected pyrites from Spanish Mountain. Position of the laser spot analyses is shown in red. Note the pyrite cores have higher Au and As ppm values than the overgrowth zones.

enrichment in the Devonian carbonaceous sediments referred to as "sedex gold," followed by the main-stage Carlin gold event during the Tertiary, related to deformation and/or felsic igneous intrusions at depth (Seedorff, 1991; Johnston and Ressel, 2004; Cline et al., 2005). The Devonian gold event is confined to one or more metalliferous horizons in the strongly carbonaceous mudstones of the Popovich Formation (Emsbo et al.; Scott et al., in press). The diagenetic gold enrichment in the pyrite (up to 320 ppm Au, Fig. 18) is accompanied by strong enrichments in As, Cu, Ni, Mo, Se, V, Sb, Mn, Pb, and Tl (Tables 1, 3). The much later Tertiary hydrothermal event produced very fine grained pyrite, and thin pyrite rims on the preexisting pyrite, with Au up to 2,000 ppm and As to 7.4 wt percent. This later hydrothermal gold event was accompanied by Sb, Tl, Cu ± Pb, Ag enrichment in the overgrowth pyrite. The cause of this late-stage, very intense, gold enrichment is unknown, however, the thin nature of the pyrite rims (2–20 μm), and their exceptionally gold-arsenic rich nature, indicates that the hydrothermal fluid was especially enriched in Au (probably over several ppm), and the fluid pulse was short-lived.

Discussion

Comparison of trace element patterns in gold-bearing pyrite from four deposits

In comparing the chemistry of the early diagenetic and later hydrothermal pyrites across all four deposits there are a number of common features, which are summarized in Tables 2 and 3, Figures 22 and 23, and discussed briefly below.

1. The early diagenetic pyrites commonly contain a wide range of enriched trace elements compared with the later metamorphic or hydrothermal overgrowth pyrites. They also may contain a greater abundance of sulfide and silicate inclusions. The LA-ICPMS output patterns suggest that some of the trace elements in porous diagenetic pyrite (e.g., V, U, Ba, Cr) are probably concentrated in silicate and organic matrix inclusions within the pyrite.

2. Arsenic is the most abundant trace element in gold-bearing diagenetic pyrites in the four deposits, followed by Ni and Cu. Arsenic levels are in the range 500 to 14,000 ppm, Ni levels are 20 to 10,000 ppm, and Cu levels are 30 to 12,600 ppm.

3. As observed by many previous workers (e.g., Cook and Chryssoulis, 1990; Fleet et al., 1993; Mumin et al., 1994; Savage et al., 2000; Cline, 2001; Reich et al., 2005), there is a positive correlation between gold and arsenic in the pyrite of many gold deposits. The positive Au-As correlation exists for both diagenetic and hydrothermal pyrites in this study (Fig. 22A). The gold-bearing diagenetic pyrites have a more restricted range on the As-Au plot, compared to the hydrothermal pyrites. All analyzed pyrites plot below the gold saturation line for arsenian pyrite as determined by Reich et al. (2005).

4. All four deposits exhibit elevated gold in the early (diagenetic) pyrite; in the range 200 ppb to 200 ppm. Two of the deposits (Bendigo and Carlin) exhibit Au-As rims on the later hydrothermal pyrites. The other two deposits (Sukhoi Log and Spanish Mountain) have Ni-Co rims on the hydrothermal pyrite, which are depleted in As and carry no detectable Au. However these late hydrothermal pyrites at Sukhoi Log and Spanish Mountain contain inclusions of free gold associated with cracks and silicate inclusions in the pyrite.

5. The diagenetic pyrites commonly contain higher mean values of Ni, Cu, Ag, Pb, Zn, Mn, and V compared to hydrothermal pyrites (Table 3), however, the two populations show considerable overlap (Fig. 22). The diagenetic pyrites may also show elevated Mo, Se, Bi, and Te, but this appears to be province specific. For example, the Carlin district diagenetic and/or sedex pyrites are enriched in Mo and Se, whereas Bendigo diagenetic pyrites are enriched in Bi and Te.

6. The early diagenetic pyrites commonly show broad positive relationships between Au-Ni and Au-V contents (Fig. 22B-C). In contrast, the later metamorphic and/or hydrothermal pyrites commonly have lower levels of Ni and V, neither of which show a positive relationship to Au. In fact, Ni in late-stage hydrothermal pyrites shows a negative relationship to gold in the Bendigo and north Carlin samples.

Origin of chemical patterns in pyrite

The consistent trace element patterns in the early and late pyrites in the orogenic and Carlin-style deposits discussed here
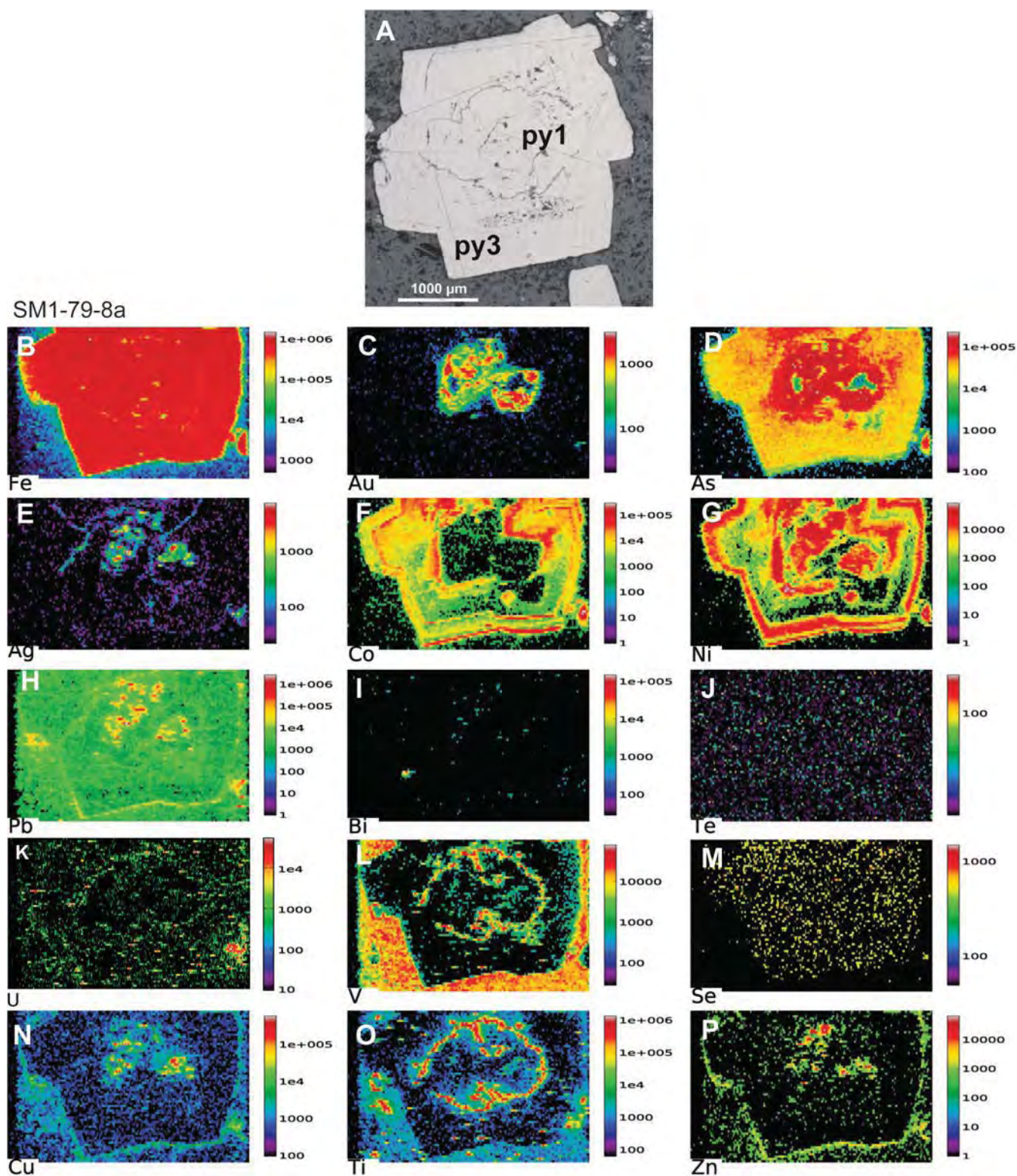
Fig. 16. LA-ICPMS images of trace elements in a pyrite composite from Spanish Mountain, sample SM1-79.8. The core of this pyrite is strongly enriched in Au, As, and Ni, with spikey inclusions of Cu, Zn, and Pb related to chalcopyrite, sphalerite, and galena microinclusions. Similar to the pyrite in Figure 11, the outermost hydrothermal rim is enriched in Ni and Co, but depleted in As and totally lacking in gold.
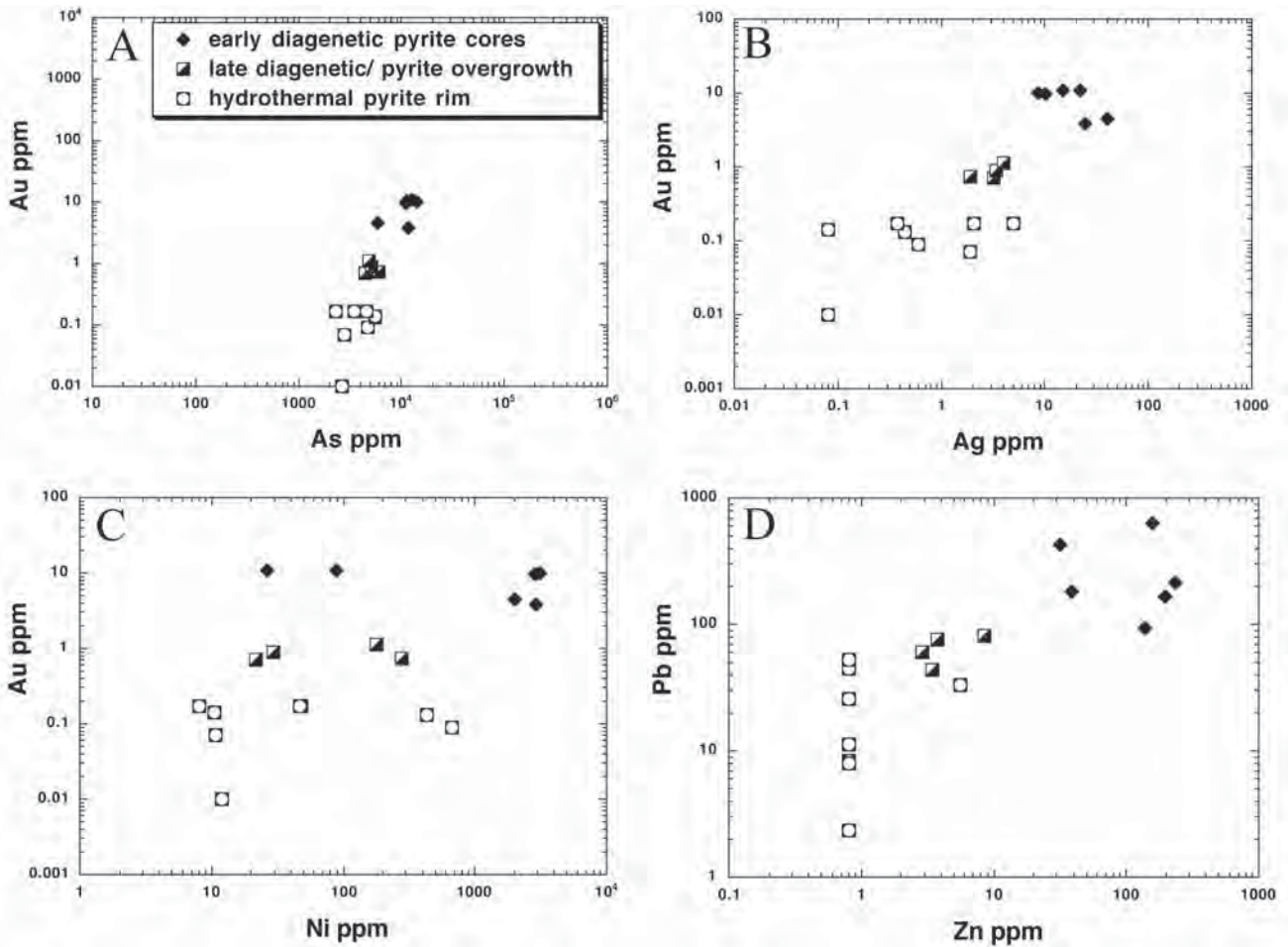
Fig. 17. Binary plots of selected trace elements in pyrite types from Spanish Mountain. Note that the diagenetic pyrite cores have elevated Au, Ag, Zn, and Pb compared with the metamorphic and/or hydrothermal rims. The highest Ni values (>1,000 ppm) occur in the center of the diagenetic cores.

indicate that common processes have occurred during pyrite formation and gold concentration for these four deposits.

The trace element suite of Ni, V, Zn, Pb, Ag, Mo, and Se in the early pyrite is the same suite of elements that are typically concentrated by organic processes during sedimentation and diagenesis of organic-rich sediments in euxinic environments (Coveney and Martin, 1983; Wood, 1996; Coveney, 2000; Alegro and Maynard, 2004; Rimmer, 2004). These elements form strong organometallic bonds, which lead to their capture from seawater onto organic matter, on and immediately below the sea floor. The weak positive correlations between Ni-Au and V-Au for our dataset of early diagenetic pyrite (Fig. 22B-C) suggests the possibility that gold was also concentrated by similar organic processes, probably involving extraction from seawater onto sedimented organic matter. During diagenesis, and growth of diagenetic arsenian pyrite, gold and many other trace elements (particularly Ni, Pb, Ag, Mo, Te, and Se) were likely partitioned from the organic matter into the arsenian pyrite, where they became trapped within the sedimentary rock. We speculate that not only is the concentration of As in the pyrite important in controlling the uptake of gold into the structure of the diagenetic pyrite (e.g., Reich et al.,

2005), but it appears from our data that the concentration of Ni may also play a role. Nickel contents in diagenetic arsenian pyrite above 1,000 ppm may be required to accommodate Au in the pyrite structure in the range 3 to 200 ppm (Fig. 22B).

The change in trace element composition of the later hydrothermal pyrites, compared to the diagenetic pyrites, is probably due to a number of factors, including the ability of the trace elements to substitute for Fe^{2+} and S^{2-} in the pyrite structure and metal availability and solubility in the hydrothermal fluid. Our data show that, except for the Carlin deposits, Pb, Zn, Cu, Ag, Ni, and Mo are commonly present at much lower levels in metamorphic and hydrothermal pyrite compared to early diagenetic pyrite. This suggests that recrystallization of diagenetic pyrite, to produce euhedral metamorphic pyrite, is accompanied by a release of certain trace elements in the pyrite structure (Large et al., 2007). At Sukhoi Log, invisible gold was released by this process to form free gold and gold telluride inclusions in later pyrite generations (Large et al., 2007). Mumin et al. (1994) reported similar remobilization of invisible gold during metamorphism in orogenic gold deposits in the Bogosu-Prestea district, Ghana. Our data suggest that the trace elements which have
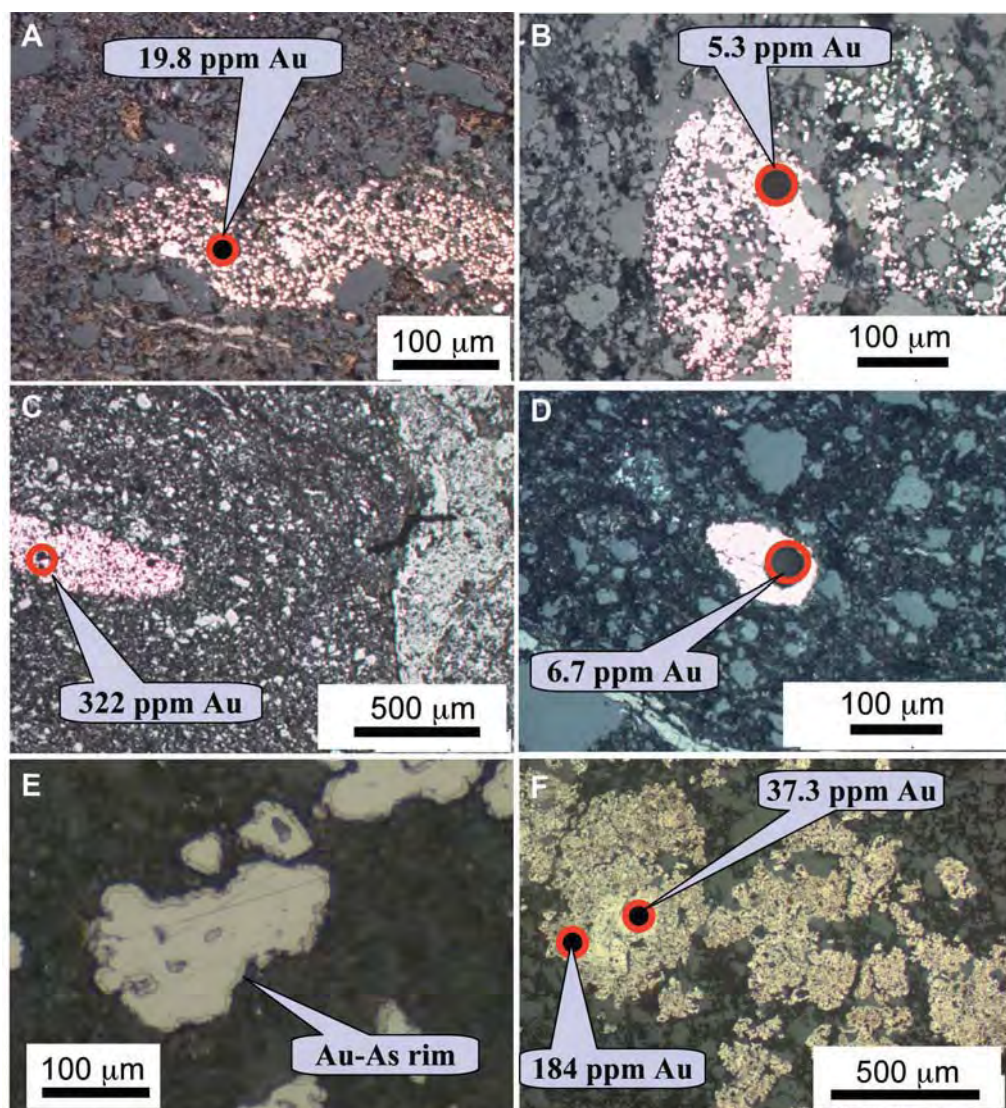
Fig. 18. Textures of pyrite types in the northern Carlin Trend, red circles indicate LA-ICPMS spots with Au analysis. A. Typical bedding-parallel cluster of diagenetic (sedex) microcrystal of pyrite in the Upper Mud Member, Popovich Formation. B.-D. Diagenetic pyrite clusters with LA-ICPMS spot analysis for Au. E. As-Au–rich main-stage 2- to 10-μm hydrothermal pyrite rims (brownish) on clear anhedral pyrite (etched with nitric acid). F. Porous, inclusion-rich, main-stage hydrothermal pyrite, surrounding 50- to 100 μm cores of less spongy pyrite. Because of the large LA-ICPMS spot size of 25 μm relative to the thin Au-As rims on the spongy pyrite, the gold value of 184 ppm has been diluted by the preore stage pyrite. Electron microprobe analyses show that the gold contents of the pyrite rims are up to >1,000 ppm, in line with results from previous workers (e.g., Kesler et al., 2003).

the ability to form limited solid-solution series with pyrite (Ni, Co, As, and Se) are not released during pyrite recrystallization and tend to concentrate in most euhedral metamorphic and hydrothermal pyrites, forming discrete growth zones in the pyrite (Figs. 3, 4, 16), possibly related to metal diffusion or fluid flow during recrystallization. This is not the case for most other trace elements (e.g., Pb, Cu, Zn, Ag, Te, and Au), due possibly to their larger ionic size and/or different charge, which leads them to form discrete mineral inclusions (galena, chalcopyrite, sphalerite, tellurides, and free gold) within the later metamorphic and/or hydrothermal pyrite.

At Sukhoi Log, Bendigo, and Spanish Mountain, the first hydrothermal pyrite to form is commonly Co rich (Figs. 4, 9,

16), followed by Co-poor pyrite. At the relatively low gold grade Sukhoi Log and Spanish Mountain deposits, the As content of the hydrothermal pyrite generally decreases toward the outer pyrite rim, whereas Ni and Co increase on the rim, and there is little concentration of invisible gold in the pyrite on the rim (Fig. 23). This contrasts with the higher gold grade Carlin and Bendigo deposits, where As and Au increase dramatically on the pyrite outer rim, but Co is depleted or absent. This suggests a fundamental difference in gold concentration and timing based on trace element zonation patterns in the pyrite from the two lower grade (<2.5 g/t Au mean grade) and two higher grade (>3 g/t Au mean grade) deposits.
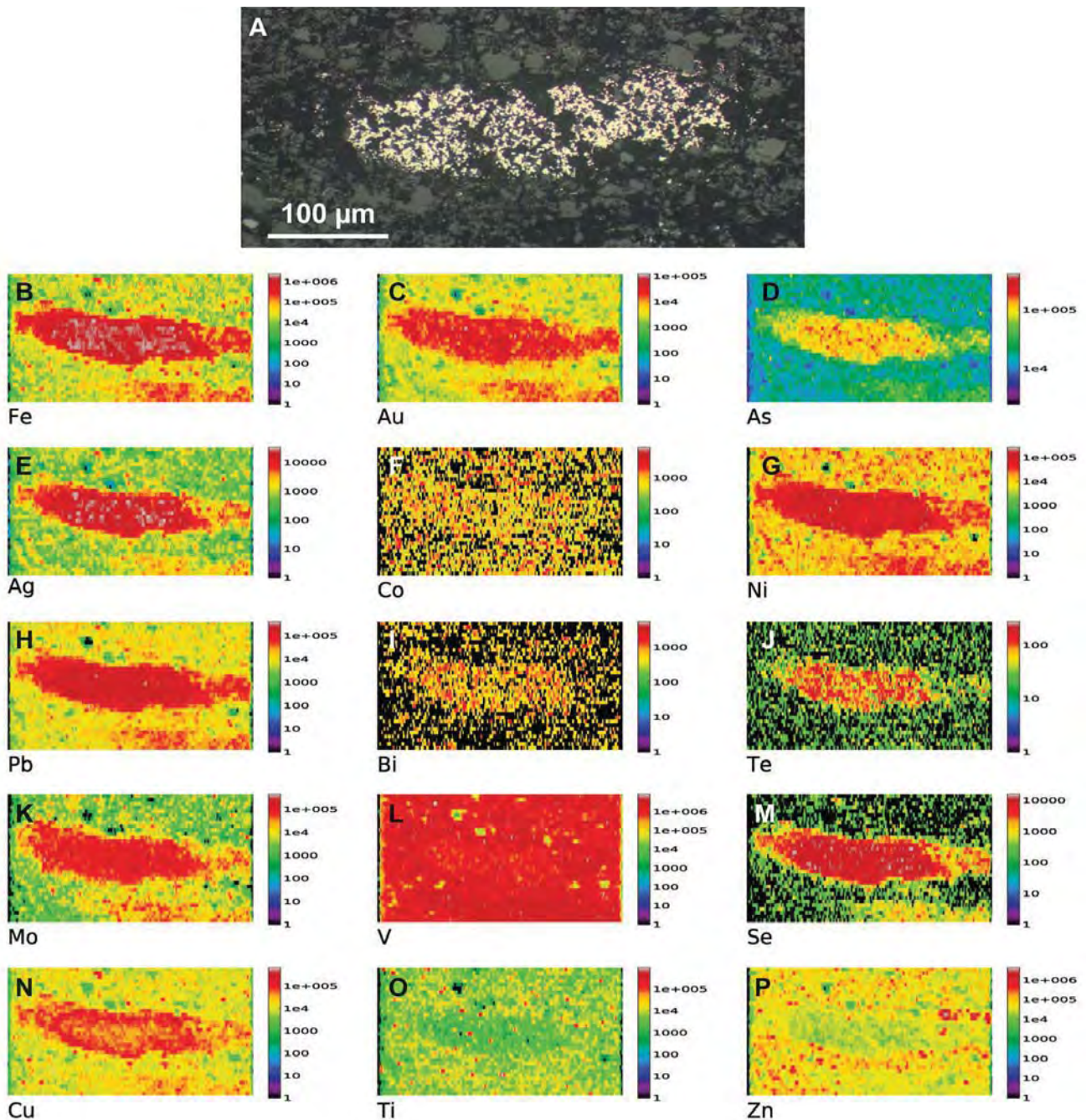
Fig. 19. LA-ICPMS images of trace elements in diagenetic pyrite from the metalliferous horizon in the Upper Mud unit, Rodeo mine, Carlin Trend, sample R11-156-4-255. Bedding-parallel diagenetic aggregate of pyrite microcrystals 300 μm long by 90 μm wide. The pyrite aggregate is enriched in Au, As, Ag, Ni, Pb, Te, Mo, Se, and Cu, typical of sedex-Au diagenetic pyrite. Zn, V, and Au are also enriched in the organic-rich sediment matrix surrounding the pyrite aggregate. Another parallel zone of Fe, Au, Pb, Ni, Mo, and Cu enrichment at the base of the frame is related to a diagenetic pyrite nodule detected by the LA-ICPMS but below the surface of optical imaging.

Although all four deposits show an early concentration of gold in diagenetic arsenian pyrite within the organic-rich sediments, gold concentration associated with basin inversion, metamorphism, deformation, and hydrothermal fluid flow has been different. At Sukhoi Log and Spanish Mountain deformation and metamorphism has led to the release of invisible gold from early diagenetic arsenian pyrite, to form free gold and gold tellurides in later generations of metamorphic and/or hydrothermal pyrite, which show a decrease in As content toward the end of the hydrothermal event. At Carlin, the later hydrothermal pyrite becomes progressively enriched in arsenic and gold, with the most gold-arsenic rich pyrite forming
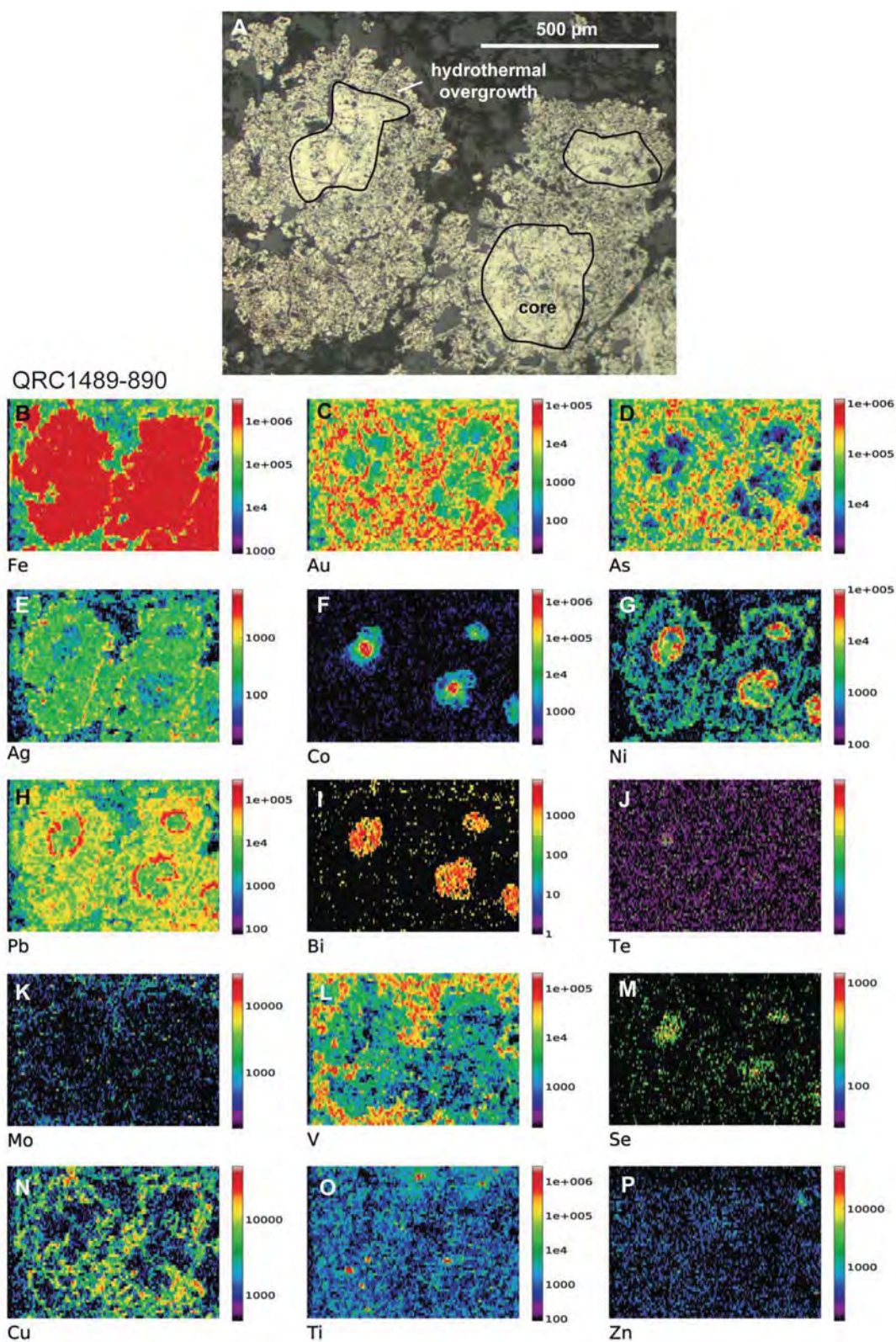
Fig. 20. LA-ICPMS images of trace elements in pyrite Gold Quarry, sample QRC 1489-890.5. Spongy network of pyrite from the gold-rich main-stage Carlin event surrounding preexisting subhedral pyrite cores. The 200-μm pyrite cores show Co-Ni-Pb enrichment and zonation but are lacking in Au and As. The thick spongy pyrite rims exhibit a complex "lacy" texture and are enriched in Au, As, Cu, Pb, and Ag.
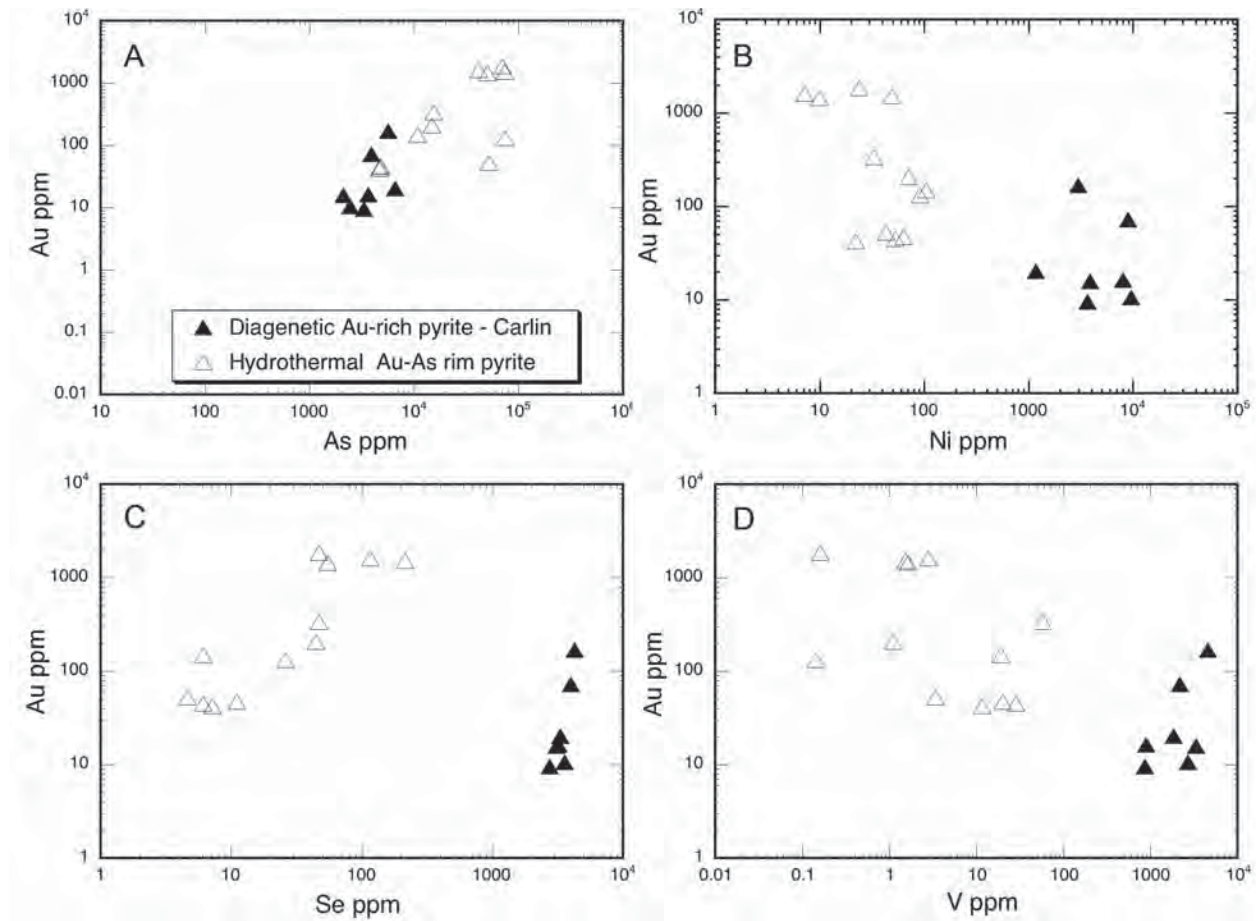
Fig. 21. Binary plots of selected trace elements in pyrite types from northern Carlin Trend. Diagenetic sedex pyrite contains elevated V, Se, and Ni but less As and Au, compared with the main-stage hydrothermal pyrite.

the outer rim, indicating an intense gold climax probably close to the final stages of deformation and related hydrothermal fluid flow. At Bendigo, hydrothermal pyrite in the sedimentary host rocks also has an Au-As rim, again suggesting gold climax toward the end of deformation, similar to Carlin. However, gold in the quartz vein saddle reefs at Bendigo is nuggety free gold, probably due to a lack of Fe for sulfidation in the quartz-rich reef structures.

Pyrite trace element evolution and gold refining

The LA-ICPMS spot data and maps show a systematic trace element evolution in the pyrite paragenesis for the four deposits. Three main stages are recognized:

Stage 1: Early sediment diagenesis; most trace elements (Cu, Pb, Zn, Co, Ni, Mn, V, Mo, As, Bi, Au, Ag, Se, Te) are "invisible" being locked in diagenetic pyrite as (1) nano-scale particles, (2) within the pyrite structure, or (3) within organic matter intimately intergrown with the pyrite. These pyrites commonly have a high Ag/Au, V/Al, and Ni/Co ratio.

Stage 2: Late diagenesis to early metamorphism leads to recrystallization of most stage 1 pyrite, and deposition of new overgrowth stage 2 pyrite. Some of the Cu, Pb, Zn, Mn, V, Ni, Mo, Au, Ag, and Te are released from stage 1 pyrite during

recrystallization to form discrete mineral phases (chalcopyrite, Ag-Bi galena, sphalerite, Ni pyrrhotite, free gold, Au-bearing tellurides), which develop as inclusions within or around the margins of stage 2 pyrite. This process of cleaning or refining the pyrite leads to different trace element ratios between stages 1 and 2 pyrites. The stage 2 event could not be recognized in the north Carlin samples.

Stage 3: Hydrothermal fluid flow late during deformation leads to further recrystallization of previous pyrite stages, with growth of stage 3 pyrite over some of the preexisting stages 1 and 2 pyrites. Except for Carlin, these stage 3 pyrites are commonly course grained, euhedral, and trace element poor, but may exhibit zonation in As, Co, and Ni. At Sukhoi Log and Spanish Mountain, As contents of the hydrothermal stage 3 pyrite vary from 980 to 5,500 ppm, with a mean of 3,300 ppm As. Invisible gold contents are correspondingly low (0.01–1 ppm), suggesting that the late metamorphic hydrothermal fluids were relatively low in As and Au. This contrasts with Carlin and Bendigo where the late-stage hydrothermal fluids were As-Au-rich and precipitated strongly enriched pyrite rims (e.g., over 5,000 ppm Au on the pyrite rims at Screamer; Kesler et al., 2003).

A number of key questions are yet to be resolved, in particular, why do Carlin and Bendigo hydrothermal pyrites have
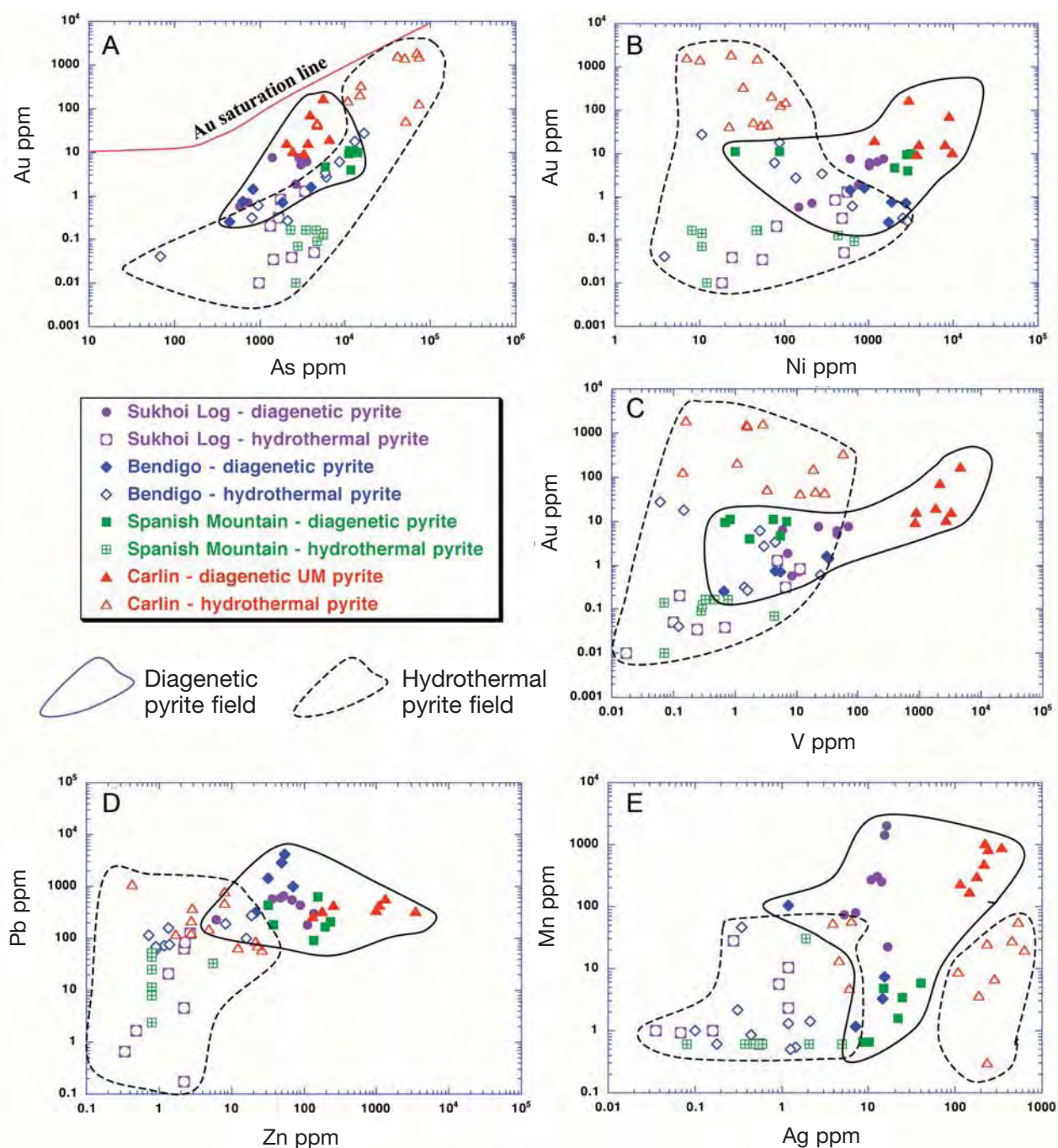
Fig 22. Binary plots of selected trace elements in pyrite from Sukhoi Log, Bendigo, Spanish Mountain, and northern Carlin Trend. A. Au-As. B. Au-Ni. C. Au-V. D. Pb-Zn.

late-stage Au-As rims, whereas Sukhoi Log and Spanish Mountain pyrites do not? and why are Carlin pyrite rims so thin and gold-arsenic enriched compared with other sediment-hosted ores? The answers most likely relate to a combination of factors, including (1) the As-Au content of the primary diagenetic pyrite-bearing sedimentary source rocks, (2) the mechanisms of release of Au and As from the sediments, (3) the nature of deformation and fluid flow, and (4) the

chemistry of the hydrothermal fluids and related Au and As transport mechanisms. In the Carlin district, injection of gold-rich fluids from Tertiary intrusions may also be a significant factor not considered here (e.g., Cline et al., 2005).

Gold mass-balance considerations

Another key question to emerge from this study is whether the gold concentrated in diagenetic pyrite within the carbonaceous
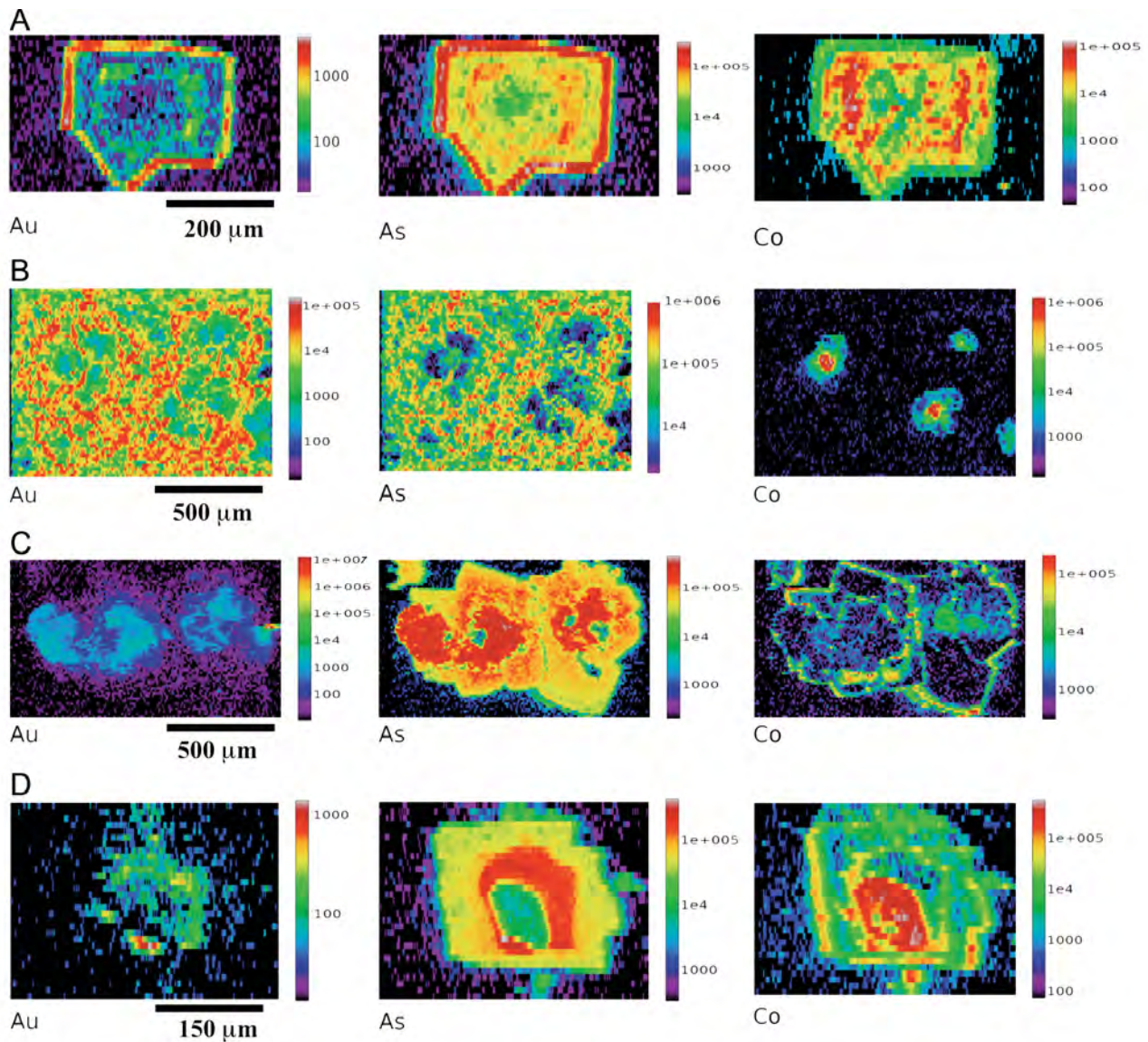
Fig 23. Comparison of Au, As, and Co zonation in sediment-hosted pyrite from (A) Bendigo, (B) Gold Quarry, Carlin, (C) Spanish Mountain, and (D) Sukhoi Log. Pyrite from Bendigo and Gold Quarry has rims enriched in Au-As but depleted in Co. In contrast pyrite from Spanish Mountain and Sukhoi Log has Au-As enriched toward the core of the pyrite, rather than the metamorphic and/or hydrothermal rim. The rims exhibit lower As but elevated Co.

shales associated with each of these four deposits could actually be the ultimate source for gold in the deposits. Our data, based on 26 gold-bearing diagenetic pyrites in selected carbonaceous shales from the four deposits (Table 1), shows a range from 0.26 to 169 ppm Au with a mean of 15.2 ppm and median of 6.2 ppm Au. If we assume the sediments prior to deformation and hydrothermal activity contained only 0.4 wt percent diagenetic pyrite (the content for average shale, Wedephol, 1995) and that the pyrite had the median value of 6 ppm Au measured in our samples, then the average initial whole-rock gold content of the sediments would have been 24 ppb Au. Assuming 80 percent of this gold is leached from the sediments during deformation and hydrothermal fluid flow, 1.54 Moz of gold could be generated per cubic kilometer of

sediments. Based on the gold resources of the four deposits and/or districts considered here, the total volumes of sediment required to source the gold in each district is shown to range from 1.7 km³ for Spanish Mountain to 32.5 km³ for the deposits on the north Carlin Trend (Table 4). These volumes of sediments are not unreasonable and only represent a small percentage of available sediments in the four sedimentary basins concerned. For example, the Early to Middle Ordovician turbidite package in the Bendigo zone in central Victoria constitute over 80,000 km³ of potential gold source rocks, compared with a volume of 11.7 km³ required to form the quartz gold reefs in the Bendigo deposit, given the above assumptions about primary gold content of the sediments.

TABLE 4. Volume of Sediments Needed to Form Some Major
Sediment-Hosted Gold Deposits and/or Districts,
Assuming Gold is Sourced from Sediments

Deposit/district	Gold resource (Moz)	Sediment Au (content in ppb)	Volume of required source sediments (km³)
Sukhoi Log	30	24[1]	19.5
Bendigo district	18	24	11.7
Spanish Mountain	2.6	24	1.7
North Carlin Trend	50	24	32.5

[1] Based on 0.4 wt percent diagenetic pyrite carrying 6 ppm Au (or, e.g., 2.0 wt % diagenetic pyrite carrying 1.2 ppm Au).

In making these mass-balance estimates, the assumptions above may be considered to be somewhat conservative, in particular the low primary diagenetic pyrite content of 0.4 wt percent assumed for the sedimentary rocks. Carbonaceous shales commonly contain considerably more diagenetic pyrite, for example, the USGS standard black shale SDO-1 contains about 10 wt percent pyrite (Huyck, 1989). Strongly pyritic carbonaceous sediments of this type may have the capacity to be far better source rocks for gold.

Conclusions

This study demonstrates the power of LA-ICPMS trace element imaging of pyrite as a rapid and robust method of providing information on the timing of gold mineralization in relationship to diagenetic, metamorphic, and hydrothermal pyrite growth for sediment-hosted gold deposits. The study of pyrite trace element zonation highlights the importance of multistage concentration of gold in the genesis of major sediment-hosted gold deposits (e.g., Hutchinson, 1975, 1993). The concentration of invisible Au, with Ni, in early diagenetic arsenian pyrite in carbonaceous black shales, as described in each of the four study areas, is proposed as a fundamental process in the later generation of orogenic and Carlin-style gold deposits. During black shale sedimentation, regional and local exhalation of Au-As–bearing basinal fluids (Emsbo et al., 1999; Wood and Large, 2007) can lead to the elevation of gold and arsenic in seawater and subsequent capture by organic matter on the sea floor. The synsedimentary gold concentrated in this manner, becomes the source for later gold reconcentrated by metamorphic and/or hydrothermal processes during basin inversion. Rather than gold being sourced from considerable depth due to metamorphic devolatilization (Kerrich and Fryer, 1979; Phillips et al., 1987) from the mantle (Perring et al., 1987; Barley and Groves, 1990) or from deep magmas (Burrows and Spooner, 1985; Goldfarb et al., 2004), we suggest that the source of the gold is organic-rich black shales and turbidites within the basin, below or lateral to the ore deposits. During deformation, the gold is remobilized from organics and diagenetic arsenian pyrite in the black shales to become concentrated in structural sites such as saddle reefs, breccia zones, and shear zones to form orogenic or Carlin-style deposits.

REFERENCES

Algeo, T.J., and Maynard, J.B., 2004, Trace-element behaviour and redox facies in core shales of Upper Pennsylvanian Kansas-type cyclothems: Chemical Geology, v. 206, p. 289–318.

Bakken, B.M., Hochella, M.F., Jr, Marshall, A.F., and Turner A.M., 1989, High resolution microscopy of gold in unoxidized ore from the Carlin mine, Nevada: ECONOMIC GEOLOGY, v. 84, p. 171–179.

Barley, M.E., and Groves, D.I., 1990, Deciphering the tectonic evolution of Archaean greenstone belts: the importance of contrasting histories to the distribution of mineralization in the Yilgarn craton, Western Australia: Precambrian Research, v. 46, p. 2–20.

Benzaazoua, M., Marion, P., Robaut, F., and Pinto, A., 2007, Gold-bearing arsenopyrite and pyrite in refractory ores: Analytical refinements and new understanding of gold mineralogy: Mineralogical Magazine, v. 71, p. 122–142.

Burrows, D.R., and Spooner, E.T.C., 1985, Generation of an Archean H_2O-CO_2 fluid enriched in Au, W and Mo by fractional crystallization in the Mink Lake intrusion, NW Ontario [abs.]: Geological Society of America Abstracts with Porgrams, v. 17, p. 536.

Butler, I.B., and Rickard, D., 2000, Framboidal pyrite formation via the oxidation of iron (II) monosulfide by hydrogen sulphide: Geochimica et Cosmochimica Acta, v. 64, p. 2665–2672.

Buyak, V.A., and Khmelevskaya, N.M., 1997, Sukhoy Log, one of the greatest gold deposits in the world: Genesis, distribution patterns, prospecting criteria, Vladivostok: Dalnauka, 156 p. (in Russian).

Cabri, L.J., Chryssoulis, S.L., Devilliers, J.P.R., Laflamme, J.H.G., and Buseck, P.R., 1989, The nature of invisible gold in arsenopyrite: Canadian Mineralogist, v. 27, p. 352–362.

Chang, Z., Large, R.R., and Maslennikov, V., 2008, Sulfur iotopes in sediment-hosted orogenic gold deposits: Evidence for an early timing and a seawater sulfur source: Geology, v. 2008, December issue, p. 971–974.

Chouinard, A., Paquette, J., and Williams-Jones, E., 2005, Crystallographic controls on trace-element incorporation in auriferous pyrite from Pascua epithermal high-sulfidation deposit, Chile-Argentina: Canadian Mineralogist, v. 43, p. 951–963.

Cline, J.S., 2001, Timing of gold and arsenic sulfide mineral deposition at the Getchell Carlin-type gold deposit, north central Nevada: ECONOMIC GEOLOGY, v. 96, p. 75–89.

Cline, J.S., Shields, D., Riciputi, L., Fayek, M., Copp, T.L., Muntean, J., and Hofstra, A.H., 2003, Trace element and isotope microanalyses support a deep ore fluid source at the Getchell Carlin-type gold deposit, northern Nevada [abs.]: Geological Society of America Abstracts with Programs, v. 35, no. 6, p.358.

Cline, J.S., Hofstra, A., Munteau, J., Tosdal, D., and Hickey, K., 2005, Carlin-type gold deposits in Nevada: Critical geologic characteristics and viable models: ECONOMIC GEOLOGY 100TH ANNIVERSARY VOLUME, p. 451–484.

Cook, N.J., and Chryssoulis, S.L., 1990, Concentrations of invisible gold in the common sulfides: Canadian Mineralogist, v. 28, p. 1–16.

Coveney, R.M., 2000, Metalliferous shales and the role of organic matter, with examples from China, Poland, and the United States: A review: ECONOMIC GEOLOGY, v. 95, p. 251–280.

Coveney, R.M., and Martin, S.P., 1983, Molybdenum and other heavy metals of the Mecca Quarry and Logan Quarry shales: ECONOMIC GEOLOGY, v. 78, p. 132–149.

Cox, S.F., Sun, S.S., Etheridge, M.A., Wall, V.J., and Potter, T.F., 1995, Structural and geochemical controls on the development of turbidite-hosted

gold quartz vein deposits, Wattle Gully mine, central Victoria, Australia: ECONOMIC GEOLOGY, v. 90, p. 1722–1746.

Craig, J.R., Vokes, F.M., and Solberg, T.N., 1998, Pyrite: Physical and chemical textures: Mineralium Deposita, v. 34, p. 82–101.

Danyushevsky, L.V., Robinson P., Gilbert, S., Norman, M., Large, R., McGoldrick, P., and Shelley, J.M.G., A technique for routine quantitative multi-element analysis of sulphide minerals by laser ablation ICP-MS: Geochemistry: Exploration, Environment, Analysis (in press).

Deditius, A. P., Utsunomiya, S., Ewing, R.C., and Kesler, S.E., 2009, Nanoscale "liquid" inclusions of As-Fe-S in arsenian pyrite: American Mineralogist, v. 94, p. 391–394.

Distler, V.V., Yudovskaya, M.A., Mitrofanov, G.L., Prokof'ev, V.Y., and Lishnevskiy, E.N., 2004, Geology, composition and genesis of the Sukhoi Log noble metals deposit, Russia: Ore Geology Reviews, v. 24, p. 7–44.

Emsbo, P., Hutchinson, R.W., Hosftra, A.H., Volk, J.A., Bettles, K.H., Baschuk, G.J., Collins, T.M., Lauha, E.A., and Borhauer, J.L., 1997, Newly discovered Devonian sedex-type base and precious metal mineralization, northern Carlin Trend, Nevada: Society of Economic Geologists Guidebook Series, v. 28, p. 109–118.

Emsbo, P., Hutchinson, R.W., Hosftra, A.H., Volk, J.A., Bettles, K.H., Baschuk, G.J., and Johnson, C.A., 1999, Syngenetic Au on the Carlin Trend: Implications for Carlin-type deposits: Geology, v. 27, p. 59–62.

Emsbo, P., Hofstra, A.H., Lauha, E.A., Griffin, G.L., and Hutchinson, R.W., 2003, Origin of high-grade gold ore, source of ore fluid components, and genesis of the Meikle and neighboring carlin-type deposits, northern Carlin Trend, Nevada: ECONOMIC GEOLOGY, v. 98, p.1069–1105.

Fleet, M.E., Maclean, P.J., and Barbier J., 1989, Oscillatory-zoned As-bearing pyrite from strata-bound and stratiform gold deposits: An indicator of ore fluid evolution: ECONOMIC GEOLOGY MONOGRAPH 6, p. 356–362.

Fleet, M.E., Chryssoulis, S.L., Maclean, P.J., Davidson, R., and Weisener, G.G., 1993, Arsenian pyrite from gold deposits—Au and As distribution investigated by SIMS and EMP, and color staining and surface oxidation by XPS and LIMS: Canadian Mineralogist, v. 31, p. 1–17.

Folk, R.L., 2005, Nannobacteria and the formation of framboidal pyrite: Textural evidence: Journal of Earth System Science, v. 114, p. 369–374.

Goldfarb, R.J., Ayuso, R., Miller, M.L., Ebert, S.W., Marsh, E.E., Petsel, S.A., Miller, L.D., Bradley, D., Johnson, C., and McClelland, W., 2004, The Late Cretaceous Donlin Creek deposit, southwestern Alaska—controls on epithermal formation: ECONOMIC GEOLOGY, v. 99, p. 642–671.

Griffin, W.L., Ashley, P.M., Ryan, C.G., Sie, S.H., and Suter, G.F., 1991, Pyrite geochemistry in the North Arm epithermal Ag-Au deposit, Queensland, Australia—a proton microprobe study: Canadian Mineralogist, v. 29, p. 185–198.

Groves, D.I., Goldfarb R. J., Gebre-Mariam, M., Hagemann, S.G., and Robert, F., 1998, Orogenic gold deposits: A proposed classification in the context of their crustal distribution and relationship to other gold deposit types: Ore Geology Reviews, v. 13, p. 7–27.

Groves, D.I., Goldfarb, R.J., Knox-Robinson, C.M., Ojala, J., Gardoll, S., Yun, G.Y., and Holyland, P., 2000, Late kinematic timing of orogenic gold deposits and significance for computer-based exploration techniques with emphasis on the Yilgarn Block, Western Australia: Ore Geology Reviews, v. 17, p.1–38.

Hagemann, S.G., and Cassidy, K.F., 2000, Archean orogenic lode gold deposits: Reviews in Economic Geology, v.13, p. 9–68.

Heiligmann, M., Williams-Jones, A.E., and Clark, J.R., 2008, The role of sulfate-sulfide-oxide-silicate equilibria in the metamorphism of hydrothermal alteration at the Hemlo gold deposit, Ontario: ECONOMIC GEOLOGY, v. 103, p. 335–351.

Hofstra, A.H., and Cline, J.S., 2000, Characteristics and models for Carlin-type gold deposits: Reviews in Economic Geology, v. 13, p. 162–221.

Huston, D.L., Sie, S.H., Suter, G.F., Cooke, D.C., and Both, R.A., 1995, Trace elements in sulfide minerals from eastern Australian volcanic-hosted massive sulfide deposits: Part 1. Proton microprobe analyses of pyrite, chalcopyrite and sphalerite: ECONOMIC GEOLOGY, v. 90, p. 1167–1196.

Hutchinson, R.W., 1975, Lode gold deposits: the case for volcanogenic derivation: Gold and Money Session and Gold Technical Session, 5th, Pacific Northwest Metals and Minerals Conference, Portland, Oregon, Proceedings, p. 64–105.

——1993, A multi-stage, multi-process genetic hypothesis for greenstone-hosted gold lodes: Ore Geology Reviews, v. 8, p. 349–382.

Huyck, H.L.O., 1989, When is a metalliferous black shale, not a black shale?: U.S Geological Survey Circular 1058, p. 42–56.

Johnston, M.K., and Ressel, M.W., 2004, Controversies on the origin of world-class gold deposits, Part 1: Carlin-type gold deposits in Nevada-Carlin-type

and distal disseminated Au-Ag deposits: Related distal expressions of Eocene intrusive centers in north-central Nevada: Society of Economic Geologists Newsletter, v. 59, p. 12–14.

Kerrich, R., and Fryer, B.J., 1979, Archean precious-metal hydrothermal systems, Dome mine, Abitibi greenstone belt: II. REE and oxygen isotope relations: Canadian Journal of Earth Sciences, v. 16, p. 440-458.

Kesler, S.E., Fortuna, J., Ye, Z., Alt, J.C., Core, D.P., Zohar, P., Borhauer, J., and Chryssoulis, S., 2003, Evaluation of the role of sulfidation in deposition of gold, Screamer section of the Betze-Post Carlin-type deposit, Nevada: ECONOMIC GEOLOGY, v. 98, p.1137–1157.

Large, R.R., Maslennikov, V., Robert, F., Danyushevsky, L.V., and Chang, Z., 2007, Multistage sedimentary and metamorphic origin of pyrite and gold in the giant Sukhoi Log deposit, Lena gold province, Russia: ECONOMIC GEOLOGY, v. 102, p. 1232–1267.

Li, X., Kwak, T.A.P., and Brown, R.W., 1998, Wall-rock alteration in the Bendigo gold ore field, Victoria, Australia: Uses in exploration: Ore Geology Reviews, v. 13, p. 381–406.

Longerich, H.P., Jackson, S.E., and Gunther, D., 1996, Laser ablation inductively coupled plasma mass spectrometric transient signal data acquisition and analyte concentration calculation: Journal Analytical Atomic Spectrometry, v. 11, p. 899–904.

Meffre, S., Large, R.R., Scott, R., Woodhead, J., Chang, Z., Gilbert, S.E., Danyushevsky, L.V., Maslennikov, V., and Hergt, J., 2008, Age and pyrite Pb-isotopic composition of the giant Sukhoi Log sediment-hosted gold deposit, Russia: Geochimica et Cosmochimica Acta, v. 72, p. 2377–2391.

Morse, J.W., and Luther, G.W., 1999, Chemical influences on trace metal-sulfide interactions in anoxic sediments: Geochimica et Cosmochimica Acta, v. 63, p. 3372–3378.

Mumin, A.H., Fleet, M.E., and Chryssoulis, S.L., 1994, Gold mineralisation in As-rich mesothermal gold ores of the Bogosu-Prestea mining district of the Ashanti gold belt, Ghana: Remobalization of "invisible' gold: Mineralium Deposita, v. 29, p. 445–460.

Panteleyev, A., Bailey, D.G., Bloodgood, M.A., and Hancock, K.D., 1996, Geology and mineral deposits of the Quesnel River-Horsefly map area, central Quesnel trough, British Columbia (NTS map sheets 93A/5, 6, 7, 11, 12, 13; 93B/9, 16; 93G/1; 93H/4): BC Ministry of Energy, Mines and Petroleum Resources, Geological Survey Branch, Bulletin 97, 156 p.

Perring, C.S., Groves, D.I., and Ho, S.E., 1987, Constraints on the source of auriferous fluids for Archaean gold deposits: Geology Department and Extension Service, University of Western Australia Publication, v. 11, p. 287–306.

Phillips, G.N., Groves, D.I., and Brown, I.J., 1987, Source requirements for the Golden Mile, Kalgoolie: Significance to the metamorphic replacement model for Archean gold deposits: Canadian Journal of Earth Sciences, v. 24, p. 1642–1651.

Phillips, G.N., Hughes, M.J., Arne, D.C., Bierlein, F.P., Carey, S.P., Jackson, T., and Willman, C.E., 2003, Gold—historical wealth, future potential: Geological Society of Australia Special Publication 23, p. 377–432.

Ramsay, W.R.H., Bierlein, F.P., Arne, D.C., and VandenBerg, A.H.M., 1998, Turbidite-hosted gold deposits of central Victoria, Australia: Their regional setting, mineralising styles, and some genetic constraints: Ore Geology Reviews, v.13, no.1–5, p.131–151.

Reich, M., Kesler, S.E., Utsunomiya, S., Palenik, C.S., Chryssoulis, S.L., and Ewing, R., 2005, Solubility of gold in arsenian pyrite: Geochemica et Cosmochimica Acta, v. 69, p. 2781–2796.

Reimold, W.U., Przybylowicz, W.J., and Gibson, R.L., 2004, Quantitative major and trace elemental mapping by PIXE of concretionary pyrite from the Witwatersrand Basin, South Africa: X-ray Spectrometry, v. 33, p. 189–203.

Rimmer, S.M., 2004, Geochemical paleoredox indicators in Devonian-Mississippian black shales, Central Appalachian basin, USA: Chemical Geology, v. 206, p. 372–391.

Savage, K.S., Tingle, T.N., O'Day, P.A., Waychunas, G.A., and Bird, D.K., 2000, Arsenic speciation in pyrite and secondary weathering phases, Mother lode gold district Tuolumne County, California: Applied Geochemistry, v. 15, p. 1219–1244.

Schaubs, P.M., and Wilson, C.J.L., 2002, The relative roles of folding and faulting in controlling gold mineralization along the Debora anticline, Bendigo, Victoria, Australia: ECONOMIC GEOLOGY, v. 97, p. 351–370.

Schieber, J., 2002, Sedimentary pyrite: A window into the microbial past: Geology, v. 30, p. 531–534.

Scholz, F., and Neumann, T., 2007, Trace element diagenesis in pyrite-rich sediments of the Achterwasser lagoon, SW Baltic Sea: Marine Chemistry, v. 107, p. 516–532.

Scott, R.J., Large, R.R. and Bull, S., 2008, Controls on the formation of sulfide trace element signatures of sediment-hosted gold deposits: Final Report and Data Compilation DVD, Hobart, CODES, University of Tasmania, AMIRA P923.

Scott, R.J., Emsbo, P., Large, R.R., Harris, A., Bull, S.W., Gilbert, S.E., Robinson, P., Danyushevsky, L.V. and Rae, A.J., 2009, Timing and character of early gold enrichment on the northern Carlin Trend: Insights from stratigraphic setting, paragenesis, and trace element composition of pyrite in the Upper Mud Member, Devonian Popovich Formation: ECONOMIC GEOLOGY, v. 104, in press.

Seedorff, F., 1991, Magmatism, extension, and ore deposits of Eocene to Holocene age in the Great Basin—mutual effects and preliminary genetic relationships: Geology and Ore Deposits of the Great Basin Symposium, Geological Society of Nevada, Reno, Nevada, Proceedings, p. 132–178.

Teal, L., and Jackson, M., 1997, Geologic overview of the Carlin Trend gold deposits and descriptions of recent deep discoveries: SEG Newsletter 31, p.1, 12–25.

Thomas, D.E., 1953, Mineralisation and the relationship to the structure of Victoria, in Edwards, A.B., ed., Geology of Australian ore deposits: Australasian Institute of Mining and Metallurgy, p. 971–985.

Wagner, T., and Boyce, A.J., 2006, Pyrite metamorphism in the Devonian Hunsruck Slate of Germany: Insights from laser microprobe sulfur isotope analysis and thermodynamic modeling: American Journal of Science, v. 306, p. 525–552.

Wagner, T, Klemd, R., Wenzel, T., and Mattsson, B., 2007, Gold upgrading in metamorphosed massive sulfide deposits: Direct evidence from laser-ablation-inductively coupled plasma-mass spectrometry analysis of invisible gold: Geology, v. 35, p. 775–778.

Wedepohl, K.H., 1995, The composition of the continental crust: Geochimica et Cosmochimica Acta, v. 59, p. 1217–1232.

Wells, J.D., and Mullins, T.E., 1973, Gold-bearing arsenian pyrite determined by microprobe analysis, Cortez and Carlin gold mines, Nevada: ECONOMIC GEOLOGY, v. 68, p. 526–537.

Willman, C.E., 2007, Regional structural controls of gold mineralization, Bendigo and Castlemaine goldfields, central Victoria, Australia: Mineralium Deposita, v. 42, p. 449–463.

Wood, B.L., and Large R.R., 2007, Syngenetic gold in western Victoria: Occurrence, age and dimensions: Australian Journal of Earth Scences, v. 54, p. 711–732.

Wood, B.L., and Popov, N.P., 2006, The giant Sukhoi Log deposit, Siberia: Russian Geology and Geophysics, v. 47, p. 315–341.

Wood, S.A., 1996, The role of humic substances in the transport and fixation of metals of economic interest (Au, Pt, Pd, U, V): Ore Geology Reviews, v. 11, p. 1–33.

Woodhead, J.D., Hellstrom, J., Hergt, J.M., Greig, A., and Mass, R., 2007, Isotopic and elemental imaging of geological materials by laser ablation inductively coupled plasma-mass spectrometry: Geostandards and Geoanalytical Research, v. 32, p. 331–343.